Draft version May 6, 2022
Typeset using LATEX **twocolumn** style in AASTeX631

The Tidal Disruption Event AT2021ehb: the Evolution of an Ultrafast Outflow, and Origins of the X-ray/UV/Optical Emission

Yuhan Yao,[1] Muryel Guolo,[2] Dheeraj R. Pasham,[3] Marat Gilfanov,[4,5] Suvi Gezari,[6] Wenbin Lu,[7] Keith C. Gendreau,[8] Fiona Harrison,[1] S. Bradley Cenko,[8] Erica Hammerstein,[9] Matt Nicholl,[10,11] Javier A. García,[1,12] Jon M. Miller,[13] Sjoert van Velzen,[14] S. R. Kulkarni,[1] Pavel Medvedev,[4] Vikram Ravi,[1] R. Sunyaev,[4,5] and Colleagues

[1]*Division of Physics, Mathematics and Astronomy, California Institute of Technology, Pasadena, CA 91125, USA*
[2]*Department of Physics and Astronomy, Johns Hopkins University, 3400 N. Charles St., Baltimore MD 21218, USA*
[3]*Kavli Institute for Astrophysics and Space Research, Massachusetts Institute of Technology, Cambridge, MA 02139, USA*
[4]*Space Research Institute, Russian Academy of Sciences, Profsoyuznaya ul. 84/32, Moscow, 117997, Russia*
[5]*Max-Planck-Institut für Astrophysik, Karl-Schwarzschild-Str. 1, D-85741 Garching, Germany*
[6]*Space Telescope Science Institute, 3700 San Martin Drive, Baltimore, MD, 21218*
[7]*Department of Astrophysical Sciences, 4 Ivy Lane, Princeton University, Princeton, NJ 08544, USA*
[8]*Astrophysics Science Division, NASA Goddard Space Flight Center, Greenbelt, MD 20771, USA*
[9]*Department of Astronomy, University of Maryland, College Park, MD 20742, USA*
[10]*School of Physics and Astronomy, University of Birmingham, Birmingham B15 2TT, UK*
[11]*Institute for Gravitational Wave Astronomy, University of Birmingham, Birmingham B15 2TT, UK*
[12]*Dr. Karl Remeis-Observatory and Erlangen Centre for Astroparticle Physics, Sternwartstr. 7, 96049 Bamberg, Germany*
[13]*Department of Astronomy, The University of Michigan, 1085 South University Avenue, Ann Arbor, Michigan 48103, USA*
[14]*Leiden Observatory, Leiden University, Postbus 9513, 2300 RA, Leiden, The Netherlands*

ABSTRACT

We present X-ray, UV, and optical observations of the nearby (≈ 78 Mpc) tidal disruption event (TDE) AT2021ehb/ZTF21aanxhjv during its first 400 days of evolution. AT2021ehb occurs in the nucleus of a galaxy hosting a $\approx 10^7\,M_\odot$ black hole ($M_{\rm BH}$ inferred from host galaxy scaling relations). High-cadence *Swift* and *NICER* monitoring reveals a delayed X-ray brightening and a soft $\rightarrow$ hard $\rightarrow$ soft spectral transition. The hard X-ray photons up to 30 keV, generated by Compton up-scattered disk emission from a hot corona, are rarely observed to be significant in other TDEs, and indicate an asymmetric geometry. During the drastic X-ray evolution, the UV/optical luminosity stays relatively constant, and the optical spectra are devoid of broad emission features. Evidence of an ultrafast outflow (UFO) is detected by our *XMM-Newton* observation ($\delta t = 107$ days, soft state) at $v \approx -0.3c$, and joint *NICER*+*NuSTAR* observations ($\delta t = 212$, 264 days, hard state) at $v \approx -0.1c$. We infer that the UFO might be produced by a stream self-collision shock, which reprocesses a large fraction of X-ray emission into the UV/optical band. Since the bolometric luminosity of AT2021ehb reaches a maximum of $\sim 0.05 L_{\rm Edd}$ when Comptonization is the strongest, the evolution of its disk–corona system is likely different from the state transition pattern typically seen in stellar-mass black hole binaries.

Keywords: Tidal disruption (1696); X-ray transient sources (1852); Supermassive black holes (1663); Time domain astronomy (2109); High energy astrophysics (739); Accretion (14)

1. INTRODUCTION

Corresponding author: Yuhan Yao
yyao@astro.caltech.edu

A star coming too close to a massive black hole (MBH) can get disrupted by the tidal forces in a tidal disruption event (TDE; see a recent review by Gezari 2021).

The first observational evidence for TDEs came from the detection of X-ray flares from centers of quiescent galaxies during the *ROSAT* (0.1–2.4 keV) all-sky survey

(RASS) in 1990–1991 (Donley et al. 2002). The flares exhibit soft spectra that are consistent with blackbody radiation with blackbody temperatures $T_{\rm bb} \sim 10^6\,{\rm K}$ and blackbody radii $R_{\rm bb} \sim$ few $\times\, 10^{11}\,{\rm cm}$ (Saxton et al. 2020). Since 2020, the *Spektrum-Roentgen-Gamma* (*SRG*) mission (Sunyaev et al. 2021), with its sensitive eROSITA telescope (0.2–8 keV; Predehl et al. 2021) and six month cadenced all-sky surveys, has become the most prolific discoverer of TDEs in X-rays (Sazonov et al. 2021). The majority of X-ray selected TDEs are faint in the optical.

In the UV and optical sky, TDEs have been identified as blue nuclear transients from surveys such as *GALEX*, PS1, SDSS, ASASSN, PTF, iPTF, ATLAS, and ZTF. The Zwicky Transient Facility (ZTF; Bellm et al. 2019; Graham et al. 2019) is now reporting ~ 15 events per year (van Velzen et al. 2021; Hammerstein et al. 2022). In most cases, the UV/optical spectral energy distribution (SED) can be described by blackbody radiation with larger radii ($R_{\rm bb} \sim$ few $\times\, 10^{14}\,{\rm cm}$) and lower temperatures ($T_{\rm bb} \sim$ few $\times\, 10^4\,{\rm K}$) than those of X-ray discovered events. The origin of this blackbody component has been attributed to reprocessing of disk emission by an optically thick gas layer, (Metzger & Stone 2016; Roth et al. 2016; Lu & Bonnerot 2020) stream self-intersecting shocks formed as a result of general relativistic apsidal precession (Piran et al. 2015; Jiang et al. 2016), or intrinsic thermal emission from the viscously heated accretion disk (Wevers et al. 2021).

Among the UV/optically selected TDEs with simultaneous X-ray observations, ~ 20 events were detected in the X-rays. Their X-ray light curves show a wide range of diversity. For example, the X-ray emission of ASASSN-14li lags behind its UV/optical emission by one month (Pasham et al. 2017); ASASSN-15oi, AT2018fyk, and AT2019zah exhibit a gradual X-ray brightening long after the UV/optical peak (Gezari et al. 2017; Wevers et al. 2021; Hinkle et al. 2021); AT2019ehz and OGLE16aaa show extreme X-ray flares on the timescale of $\sim$ few $\times$ days (van Velzen et al. 2021; Kajava et al. 2020); while the probable neutrino emitter AT2019dsg has a rapid X-ray decline (Stein et al. 2021). Understanding the co-evolution between the X-ray and UV/optical emission may hold the key in deciphering the origin of these two components.

Mildly relativistic ($v \gtrsim 0.1c$) (disk) winds, also known as ultrafast outflows (UFOs), can be probed by high-quality X-ray spectra of X-ray loud TDEs. By detecting the blueshifted absorption or emission X-ray spectral features, UFOs have been found in 3XMM J152130.7+074916 ($\sim 0.12c$, Lin et al. 2015), ASASSN-14li ($\sim 0.2c$, Kara et al. 2018), and the jetted[1] TDE Swift J1644+57 ($\sim 0.15c$, Kara et al. 2016). Studies of such UFOs will help us understand the TDE wind launching mechanisms and the accretion flow structure. All previous TDEs with UFO detections have $L_{\rm bol} > L_{\rm Edd}$, which are consistent with radiation-driven wind under super-Eddington accretion (Dai et al. 2018).

It has been known for long that during the outburst of a stellar mass black hole X-ray binary (XRB), as the mass accretion rate ($\dot{M}_{\rm acc}$) varies, the X-ray source transitions between distinct hard/soft states, governed by the global evolution of the disk–corona system (Remillard & McClintock 2006). A major question in accretion physics is whether a similar geometry operates in the environment around MBHs. Recent studies of a sample of changing-look AGN (CLAGN) support a scale invariance nature of black hole accretion flows (Ruan et al. 2019). However, the preexisting gas and dusty torus sometimes complicate interpretation of the observables in CLAGN (Guolo et al. 2021). On the other hand, the majority of TDEs are hosted by the otherwise quiescent galaxies (French et al. 2020). Therefore, TDEs provide ideal laboratories for studying MBH accretion in different regimes (Ulmer 1999; Strubbe & Quataert 2009).

In this paper, we present an in-depth study of the X-ray, UV, and optical emission from the TDE AT2021ehb, using observations obtained from 2021 March 1 to 2022 April 11. The proximity ($z = 0.0180$) and the intrinsic high X-ray luminosity ($\sim 10^{43}\,{\rm erg\,s^{-1}}$) of this source allowed us to perform detailed X-ray spectral modeling, which enabled the detection of an UFO with different velocities at various evolutionary stages. Unlike the X-ray spectra of most other TDEs (Saxton et al. 2020; Sazonov et al. 2021), the X-ray spectrum of AT2021ehb exhibits a prominent non-thermal hard component, signifying early formation of a hot corona above the accretion disk. We are thus able to study the evolution of its disk–corona system, and find dissimilarities to XRBs.

We detail the discovery and background of AT2021ehb in §2, and outline observations in §3. We analyze the host galaxy in §4, including measurements of the central black hole mass ($M_{\rm BH}$) and the SED. We study the light curve and spectral evolution of the TDE emission in §5. We provide a discussion in §6, and conclude in §7.

2. AT2021ehb: DISCOVERY AND BACKGROUND

ZTF conducts multiple time-domain surveys using the ZTF mosaic camera (Dekany et al. 2020) on the the Palomar Oschin Schmidt 48-inch (P48) telescope. On 2021 March 1, ZTF21aanxhjv was discovered by the

[1] "Jetted TDEs" are TDEs that launch an ultra relativistic jet.

ZTF public 2-day cadence all-sky survey at $g_{\rm ZTF} = 19.10 \pm 0.22$. On 2021 March 3, it was reported to the Transient Name Server (TNS) by the ALeRCE broker (Munoz-Arancibia et al. 2021), and was given the name AT2021ehb. AT2021ehb is a nuclear transient in the galaxy WISEA J030747.82+401840.9 with a photometric redshift of $z = 0.017$ in the GLADE v2.3 catalog (Dálya et al. 2018). In this paper we adopt a spectroscopic redshift of $z = 0.0180$ (see §4.1).

On 2021 March 25, AT2021ehb passed our filter designed to select TDE candidates (van Velzen et al. 2019), and *Swift* observations were triggered while the TDE was still on the rise to peak. On 2021 March 26, we classified AT2021ehb as a TDE based on its nuclear location, persistent blue color, and bright UV emission (Gezari et al. 2021). Four *Swift* snapshots from March 26 to April 2 yielded no X-ray detections.

From 2021 April 12 to June 16, AT2021ehb was not observed due to occultation by the Sun. On 2021 June 17, ZTF observations resumed. On 2021 July 1, X-rays were detected with *Swift* (Yao et al. 2021a). Its bright X-ray emission ($\sim 10^{42}\,{\rm erg\,s^{-1}}$) and the subsequent X-ray brightening have motivated us to conduct a comprehensive monitoring campaign.

UT time is used throughout the paper. We adopt a standard ΛCDM cosmology with the matter density $\Omega_{\rm M} = 0.3$, the dark energy density $\Omega_\Lambda = 0.7$, and the Hubble constant $H_0 = 70\,{\rm km\,s^{-1}\,Mpc^{-1}}$, implying a luminosity distance to AT2021ehb of $D_L = 78.2\,{\rm Mpc}$. UV and optical magnitudes are reported in the AB system. We use the extinction law from Cardelli et al. (1989), and adopt a Galactic extinction of $E_{B-V,{\rm MW}} = 0.123$ (Schlafly & Finkbeiner 2011). Unless otherwise noted, uncertainties represent the 68% confidence intervals and upper limits are reported at 3σ. Coordinates are given in J2000.

3. OBSERVATION AND DATA REDUCTION

3.1. *ZTF Optical Photometry*

We obtained ZTF[2] forced photometry (Masci et al. 2019) in the g and the r bands using the median position of all ZTF alerts up to MJD 59550 ($\alpha =$ 03h07m47.82s, $\delta = +40^\circ18'40.85''$). We performed baseline correction following the procedures outlined in Yao et al. (2019).

The peak of the optical light curve probably occurred during Sun occultation and cannot be robustly determined. Therefore, we fitted a five-order polynomial function to the $r_{\rm ZTF}$-band observations, which suggested that the optical maximum light was around MJD $\approx$ 59321. Hereafter we use δt to denote rest-frame days relative to MJD 59321. The Galactic extinction corrected ZTF light curve is shown in Figure 1. All ZTF photometry are provided in Appendix A.1 (Table 6).

[2] https://ztfweb.ipac.caltech.edu/cgi-bin/requestForcedPhotometry.cgi

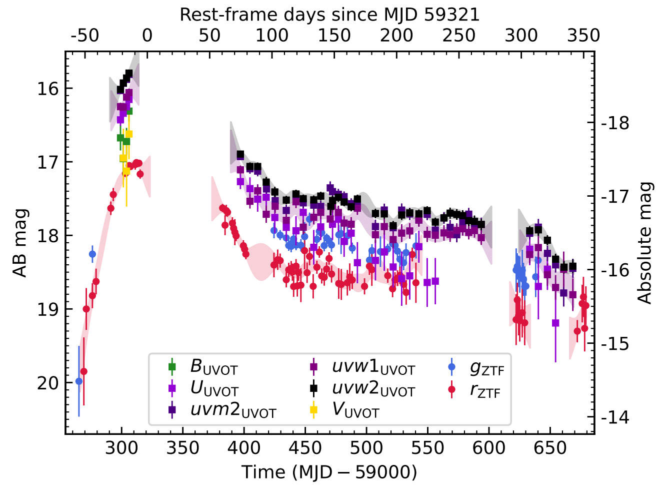

Figure 1. Optical and UV light curves of AT2021ehb. The host contribution has been removed using difference photometry (ZTF, §3.1) or subtraction of fluxes estimated from the galaxy SED (UVOT, §3.4.2). Photometry has only been corrected for Galactic extinction. The transparent lines are simple Gaussian process fits in each filter (see §5.1), where the width of the lines represent 1σ model uncertainties. For clarity, we only show the model fits in the $r_{\rm ZTF}$, $uvw1$, and $uvw2$ bands. Regions where the model uncertainty is greater than 0.3 mag are not shown.

3.2. *SEDM and LT Optical Photometry*

We obtained additional *ugri* photometry using the Spectral Energy Distribution Machine (SEDM, Blagorodnova et al. 2018, Rigault et al. 2019) on the robotic Palomar 60 inch telescope (P60, Cenko et al. 2006), and the optical imager (IO:O) on the Liverpool Telescope (LT; Steele et al. 2004). The SEDM photometry was host-subtracted using the automated pipeline `FPipe` Fremling et al. (2016). The LT photometry was host subtracted using SDSS images.

A mismatch was found to exist between the SEDM/LT gr photometry and the ZTF photometry. This is probably a result of different reference images being used. The ZTF difference photometry is more reliable since the reference images were constructed using P48 observations taken in 2018–2019. The reference images of SEDM/LT comes from SDSS images (taken in 2005), and long-term variability of the galaxy nucleus will render the difference photometry less robust. Therefore, we presented the SEDM and LT photoemtry in Appendix A.1 (Table 6), but excluded them in the following analysis.

3.3. *Optical Spectroscopy*

We obtained low-resolution optical spectroscopic observations using the Low Resolution Imaging Spectrograph (LRIS; Oke et al. 1995) on the Keck-I telescope (PIs: Ravi, Kulkarni), the Double Spectrograph (DBSP; Oke & Gunn 1982) on the 200-inch Hale telescope (PI: Kulkarni), the integral field unit (IFU; $R \approx 100$) spectrograph of SEDM (PI: Hammerstein), the De Veny Spectrograph on the Lowell Discovery Telescope (LDT; PI: Cenko). We also obtained a medium-resolution spectrum using the Echellette Spectrograph and Imager (ESI; Sheinis et al. 2002) on the Keck-II telescope (PI: Kulkarni)

The low-resolution spectra are shown in Figure 2. The instrumental details and an observing log can be found in Appendix B.

3.4. *Swift*

AT2021ehb was observed by the X-Ray Telescope (XRT; Burrows et al. 2005) and the Ultra-Violet/Optical Telescope (UVOT; Roming et al. 2005) on board *Swift* under our GO program 1619088 (as ZTF21aanxhjv; target ID 14217; PI: Gezari) and a series of time-of-opportunity (ToO) requests (PI: Yao). All *Swift* data were processed with `heasoft` v6.29c.

3.4.1. *XRT*

All XRT observations were obtained in the photon-counting mode. First, we ran `ximage` to select snapshots where AT2021ehb was detected above 3σ. For X-ray non-detections, we computed upper limits within a circular region of $30''$ centered on AT2021ehb. For X-ray detections, to calculate the background-subtracted count rates, we filtered the cleaned event files using a source region with $r_{\rm src} = 30''$, and eight background regions with $r_{\rm bkg} = 25''$ evenly spaced at $80''$ from AT2021ehb. A log of XRT observations is given in Appendix A.1 (Table 7).

We generated XRT spectra using an automated online tool[3] (Evans et al. 2009). To improve the SNR of each spectrum, we stacked consecutive observations with similar hardness ratio (HR) (see details in §5.4.5).

3.4.2. *UVOT*

The first four UVOT epochs (obsID 14217001–14217005) were conducted with UBV+All UV filters. Subsequent observations were conducted with U+All UV filters.

We measured the UVOT photometry using the `uvotsource` tool. We used a circular source region with $r_{\rm src} = 12''$, and corrected for the enclosed energy within the aperture[4]. We measured the background using two nearby circular source-free regions with $r_{\rm bkg} = 15''$. Following the procedures outlined in van Velzen et al. (2021), we estimated the host-galaxy flux in the UVOT bandpass from the population synthesis models (see §4.2). The UVOT light curves are presented in Figure 1 and provided in Appendix A.1 (Table 6).

3.5. *NICER*

AT2021ehb was observed by the Neutron Star Interior Composition Explorer (*NICER*; Gendreau et al. 2016) under Director's Discretionary Time (DDT) programs on 2021 March 26, 2021 July 2–7, and from 2021 November 13 to 2022 March 29 (PIs: Yao, Gendreau, Pasham). The *NICER* data were processed using `nicerdas` v9 (`2021-08-31_V008c`). We ran `nicerl2` to obtain the cleaned and screened event files. Background was computed using the `nibackgen3C50` tool (Remillard et al. 2022). Following the screening criteria suggested by Remillard et al. (2022), we removed GTIs with `hbgcut=0.05` and `s0cut=2.0`.

We extracted one spectrum for each obsID, excluding obsIDs with 0.3–1 keV background rate $> 0.2\,{\rm count\,s^{-1}}$ or 4–12 keV background rate $> 0.1\,{\rm count\,s^{-1}}$. Using observations bracketed by the two *NuSTAR* observations, we also produced two *NICER* spectra with exposure times of 8.2 ks and 36.6 ks, which will be jointly analyzed with the *NuSTAR* spectra (see §5.4.1 and §5.4.2).

All *NICER* spectra were binned using the optimal binning scheme (Kaastra & Bleeker 2016), and simultaneously ensured to have at least 20 counts per bin. Following the *NICER* calibration memo[5], we added systematic errors of 1.5% with `grppha`.

3.6. *XMM-Newton*

We obtained two epochs of follow-up observations with *XMM-Newton* under our Announcement of Opportunity (AO) program (PI: Gezari) on 2021 August 4 (obsID 0882590101), and 2022 January 25 (obsID 0882590901). The observations were taken in Full Frame mode with the thin filter using the European Photon Imaging Camera (EPIC; Strüder et al. 2001).

The observation data files (ODFs) were reduced using the *XMM-Newton* Standard Analysis Software (Gabriel et al. 2004). The raw data files were then processed using the `epproc` task. Since the pn instrument generally

[3] https://www.swift.ac.uk/user_objects

[4] A large aperture is chosen to make sure that all the flux of the host galaxy is captured.

[5] See https://heasarc.gsfc.nasa.gov/docs/nicer/data_analysis/nicer_analysis_tips.html.

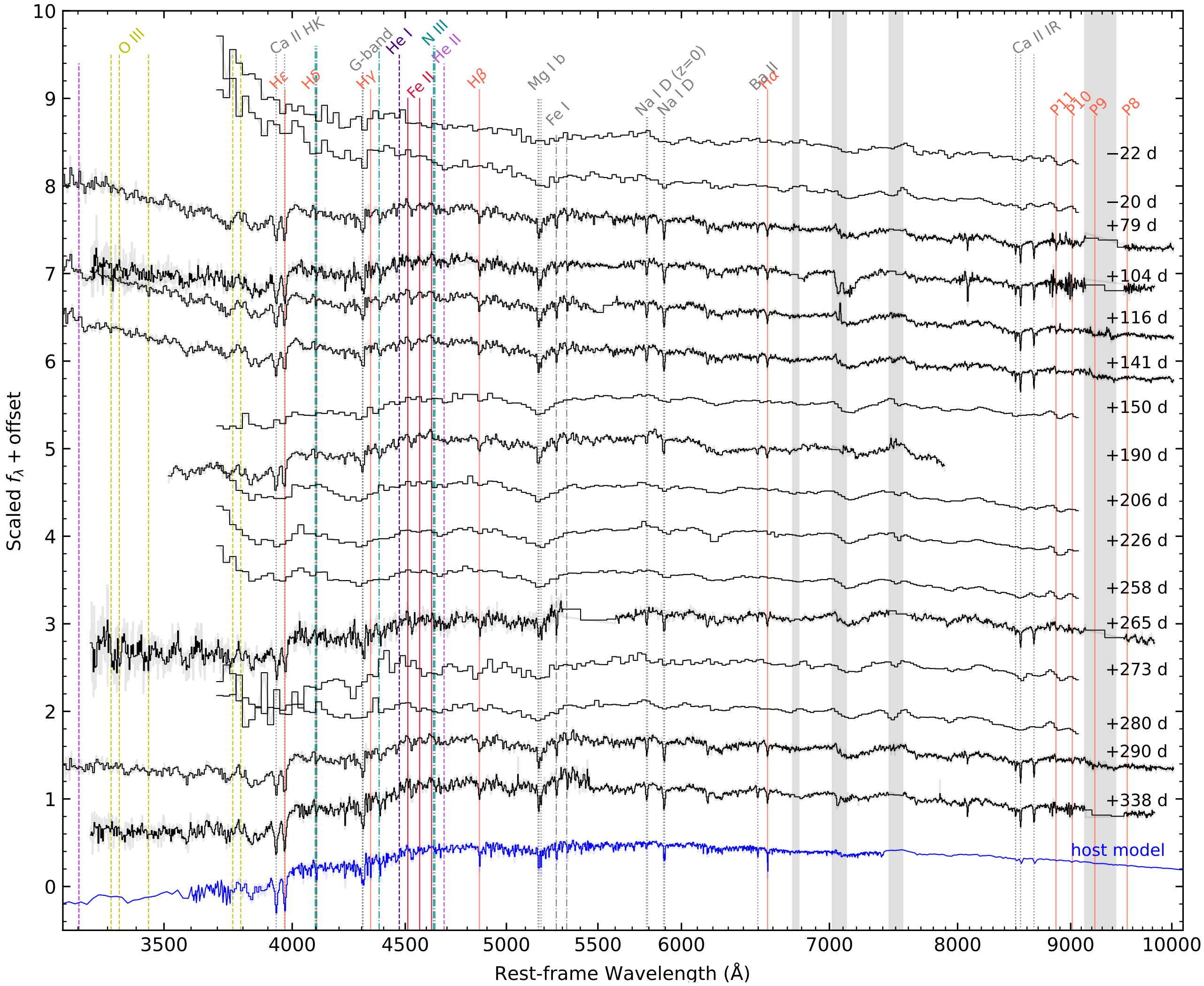

Figure 2. Optical spectroscopic evolution of AT2021ehb. The observed spectra have been corrcted for Galactic extinction. The vertical lines mark observed strong host absorption lines and spectral features common in TDEs. The vertical grey bands mark atmospheric telluric features and strong telluric features have been masked. The best-fit galaxy model is shown in the bottom (see §4.2).

has better sensitivity than MOS1 and MOS2, hereafter we only analyzed the pn data. Following the *XMM-Newton* data analysis guide, to check for background activity and generate "good time intervals" (GTIs), we manually inspected the background light curves in the 10–12 keV band. Using the `evselect` task, we only retained patterns that correspond to single and double events (`PATTERN<=4`).

The source spectra were extracted using a source region of $r_{\rm src} = 35''$ around the peak of the emission. The background spectra were extracted from a $r_{\rm bkg} = 108''$ region located in the same CCD. The ARFs and RMF files were created using the `arfgen` and `rmfgen` tasks, respectively. We groupped the spectra to have at least 25 counts per bin, and limited the over-sampling of the instrumental resolution to a factor of 5.

3.7. *SRG*

Table 1. Log of *SRG* observations of AT2021ehb.

eRASS	MJD	δt (days)	0.3–10 keV flux ($10^{-13}\,{\rm erg\,s^{-1}\,cm^{-2}}$)
1	58903.59–58904.59	−409.5	< 0.25
2	59083.36–59084.70	−232.8	< 0.23
3	59253.16–59254.16	−66.1	< 0.23
4	59442.45–59443.62	+119.9	$76.8^{+2.5}_{-2.4}$
5	59624.53–59625.70	+298.7	$30.7^{+2.4}_{-2.3}$

Note—Upper limits are at 90% confidence.

The location of AT2021ehb was scanned by the eROSITA and the Mikhail Pavlinsky ART-XC (Pavlinsky et al. 2021) telescopes on board the *Spektrum-Roentgen-Gamma* (*SRG*) satellite as part of the planned eight all-sky surveys. Hereafter eRASSn refers to the n'th eROSITA all-sky survey[6]. During eRASS4, AT2021ehb was independently identified by *SRG* as a TDE candidate. A log of *SRG* observations is given in Table 1. We groupped the eRASS4 and eRASS5 spectra to have at least 3 counts per bin.

3.8. *NuSTAR*

We obtained Nuclear Spectroscopic Telescope ARray (*NuSTAR*; Harrison et al. 2013) observations under a pre-approved ToO program (PI: Yao; obsID 80701509002) and a DDT program (PI: Yao; obsID 90801501002). The first epoch was conducted from 2021 Nov 18.8 to Nov 19.9 with an exposure time of 43.2 ks. The second epoch was conducted from 2022 Jan 10.4 to Jan 12.1 with an exposure time of 77.5 ks.

To generate the first epoch's spectra for the two photon counting detector modules (FPMA and FPMB), source photons were extracted from a circular region with a radius of $r_{\rm src} = 40''$ centered on the apparent position of the source in both FPMA and FPMB. The background was extracted from a $r_{\rm bkg} = 80''$ region located on the same detector. For the second epoch, since the source was brighter, we used a larger source radius of $r_{\rm src} = 70''$, and a smaller background radius of $r_{\rm bkg} = 65''$.

All spectra were binned first with `ftgrouppha` using the optimal binning scheme developed by Kaastra & Bleeker (2016), and then further binned to have at least 20 counts per bin.

4. HOST GALAXY ANALYSIS

Figure 3 shows the pre-TDE optical image centered on AT2021ehb, using data from the Panoramic Survey Telescope and Rapid Response System DR1 (Pan-STARRS, PS1) (Flewelling et al. 2020; Waters et al. 2020). The host galaxy appears to be close to edge-on.

4.1. *Velocity Dispersion and Black Hole Mass*

The host galaxy absorption lines are prominent in the optical spectra (see Figure 2). Using our medium-resolution ($R = 5350$) spectrum taken with Keck-II/ESI, we measured the line centers of strong absorption lines, and determined the redshift to be $z = 0.0180$.

[6] Here n runs from 1 to 8. As of April 2022, eRASS1–eRASS4 have been completed, and 38% (sky area) of eRASS5 has been completed.

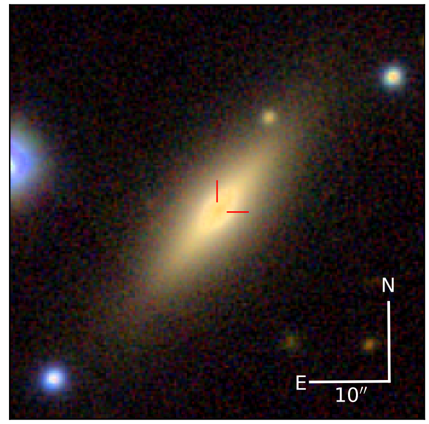

Figure 3. PS1 RGB false-color $g/i/z$ image centered on AT2021ehb.

Following previous TDE works (Wevers et al. 2017, 2019a; French et al. 2020), we measured the stellar velocity dispersion by fitting the normalized ESI spectrum (see pre-processing procedures in Appendix §B) with the penalized pixel-fitting (`pPXF`) software (Cappellari & Emsellem 2004; Cappellari 2017). `pPXF` fits the absorption line spectrum by convolving a library of stellar spectra with Gauss-Hermite functions. We adopted the ELODIE v3.1 high resolution ($R = 42000$) template library (Prugniel & Soubiran 2001; Prugniel et al. 2007).

To robustly measure the velocity dispersion and the associated uncertainties, we perform 1000 Monte Carlo (MC) simulations, following the approach adopted by Wevers et al. (2017). In each fitting routine, we mask wavelength ranges of common galaxy emission lines and hydrogen Balmer lines. The derived velocity dispersion is $\sigma = 92.9^{+5.3}_{-5.2}\,{\rm km\,s^{-1}}$ at 95% confidence interval.

According to the $M_{\rm BH}$–σ relation (Kormendy & Ho 2013), the measured σ corresponds to a black hole mass of $\log(M_{\rm BH}/M_\odot) = 7.03 \pm (0.15 + 0.29)$, where 0.29 is the intrinsic scatter of the $M_{\rm BH}$–σ relation. If adopting the Ferrarese & Ford (2005) $M_{\rm BH}$–σ relation, then $\log(M_{\rm BH}/M_\odot) = 6.60 \pm (0.20 + 0.34)$. Hereafter we adopt the result from the Kormendy & Ho (2013) relation because it includes more low mass galaxies.

We note that although the Kormendy & Ho (2013) relation was originally calibrated mainly at a $M_{\rm BH}$ regime that is too heavy to produce a TDE, recent studies show that the same relation holds in the dwarf galaxy regime (Baldassare et al. 2020).

4.2. *Host SED Model*

We constructed the pre-TDE host galaxy SED using photometry from the Sloan Digital Sky Survey (SDSS, Alam et al. 2015), the Two Micron All-Sky Survey (2MASS; Skrutskie et al. 2006), and the AllWISE cat-

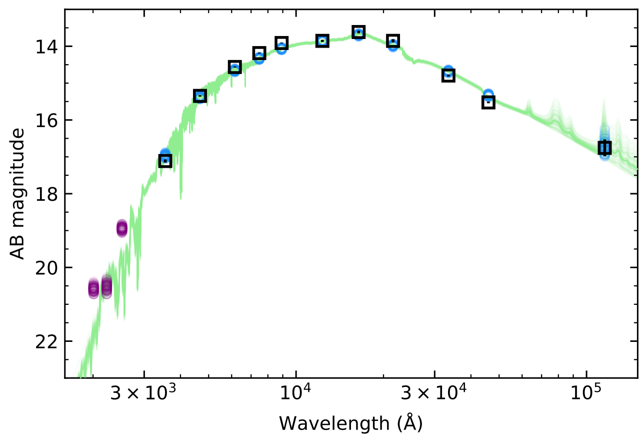

Figure 4. Host galaxy SED of AT2021ehb. The open squares are the Galactic extinction corrected host photometry. The green lines are samples from the posterior distribution of host galaxy SED models. The open circles are the synthetic host galaxy magnitude in the observed bands (shown in blue) and the all UV filters of *Swift*/UVOT (shown in purple).

alog (Cutri & et al. 2013). The photometry of the host is shown in Table 2.

Table 2. Observed photometry of the host galaxy.

Catalog	Band	$\lambda_{\rm eff}$ (nm)	Magnitude
SDSS	u	355	17.748 ± 0.019
SDSS	g	467	15.814 ± 0.003
SDSS	r	616	14.901 ± 0.002
SDSS	i	747	14.443 ± 0.003
SDSS	z	892	14.094 ± 0.004
2MASS	J	1232	13.951 ± 0.025
2MASS	H	1642	13.676 ± 0.034
2MASS	$K_{\rm s}$	2157	13.893 ± 0.043
AllWISE	$W1$	3346	14.816 ± 0.024
AllWISE	$W2$	4595	15.535 ± 0.022
AllWISE	$W3$	11553	16.756 ± 0.229

Our SED fitting approach is similar to that described in van Velzen et al. (2021). We used the flexible stellar population synthesis (`FSPS`) code (Conroy et al. 2009), and adopted a delayed exponentially declining star-formation history (SFH) characterized by the e-folding timescale $\tau_{\rm SFH}$. The `Prospector` package (Johnson et al. 2021) was utilized to run a Markov Chain Monte Carlo (MCMC) sampler (Foreman-Mackey et al. 2013). We show the best-fit model prediction of the host galaxy optical spectrum at the bottom of Figure 2.

From the marginalized posterior probability functions we obtain the total galaxy stellar mass $\log(M_*/M_\odot) = 10.18^{+0.01}_{-0.02}$, the metallicity, $\log Z = -0.57 \pm 0.04$, $\tau_{\rm SFH} = 0.19^{+0.18}_{-0.07}$ Gyr, the population age, $t_{\rm age} = 12.1^{+0.3}_{-0.6}$ Gyr, and negligible host reddening ($E_{B-V,\rm host} = 0.01 \pm 0.01$). The best-fit SED model is shown in Figure 4.

Following Gezari (2021), we use the $M_{\rm BH}$–M_* relation from Greene et al. (2020) to obtain a black hole mass of $\log(M_{\rm BH}/M_\odot) = 7.14 \pm (0.10 + 0.79)$, where 0.79 is the intrinsic scatter of the scaling relation. This is consistent with $M_{\rm BH}$ inferred from the $M_{\rm BH}$–σ relation (§4.1).

To summarize, the host galaxy of AT2021ehb has a total stellar mass of $M_* \approx 10^{10.18}\,M_\odot$ and a BH mass of $M_{\rm BH} \approx 10^{7.03}\,M_\odot$. The measured black hole mass is on the high end of the population of optically selected TDEs (French et al. 2020; Nicholl et al. 2022), and is too heavy to disrupt a white dwarf (Rosswog et al. 2009).

5. ANALYSIS OF THE TDE EMISSION

5.1. *UV/optical Photometric Analysis*

To capture the general trend of AT2021ehb's UV/optical photometric evolution, we fit the data in each filter using a combination of five-order polynomial functions and Gaussian process smoothing, following procedures described in Appendix B.4 of (Yao et al. 2020). The model fits in $r_{\rm ZTF}$, $uvw1$, and $uvw2$ are shown as semi-transparent lines in Figure 1.

We then define a set of "good epochs" close in time to actual multiband measurements, and fit a Planck function to each set of fluxes to determine the effective temperature $T_{\rm bb}$, photospheric radius $R_{\rm bb}$, and blackbody luminosity of the UV/optical emitting component $L_{\rm bb}$. We initially assume $E_{B-V,\rm host} = 0$, and then repeat the procedure under different assumptions about the host reddening. We find that the fitting residual monotonically increases as $E_{B-V,\rm host}$ increases from 0 to 0.2, suggesting negligible host reddening. Therefore, for the reminder of the discussion we assume $E_{B-V,\rm host} = 0$.

We also define a set of "ok epochs" where we only have photometric observations in the optical (or only in the UV). Due to a lack of wavelength coverage, $T_{\rm bb}$ and $R_{\rm bb}$ can not be simultaneously constraint. As such we fix the $T_{\rm bb}$ values by interpolating the $T_{\rm bb}$ evolution of "good epochs", and fit for $R_{\rm bb}$ values of "ok epochs".

The physical parameters derived from the blackbody fits are shown in Figure 5, where they are compared with a sample of recent TDEs with multiple X-ray detections. We have measured the blackbody parameters of other TDEs using the same procedures described above.

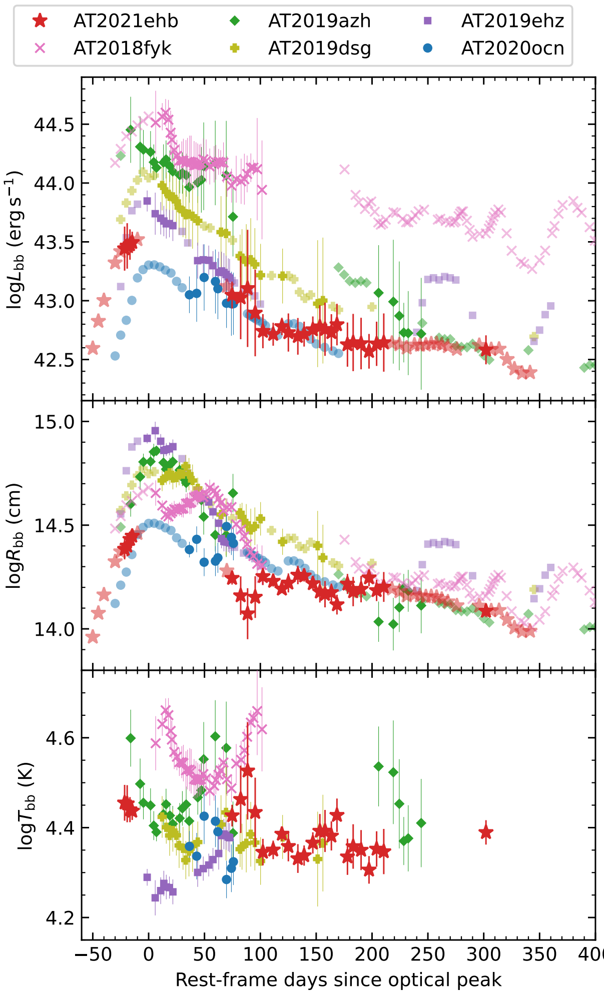

Figure 5. Evolution of the UV/optical blackbody properties of AT2021ehb compared with a sample of recent X-ray bright TDEs in the literature, including AT2018fyk (Wevers et al. 2019b, 2021), AT2019dsg (Stein et al. 2021), AT2019azh (Hinkle et al. 2021), AT2020ocn, and AT2019ehz (van Velzen et al. 2021). The results of "good epochs" (see definition in text) are shown in high-opacity colors, whereas results of "ok epochs" are shown in semi-transparent.

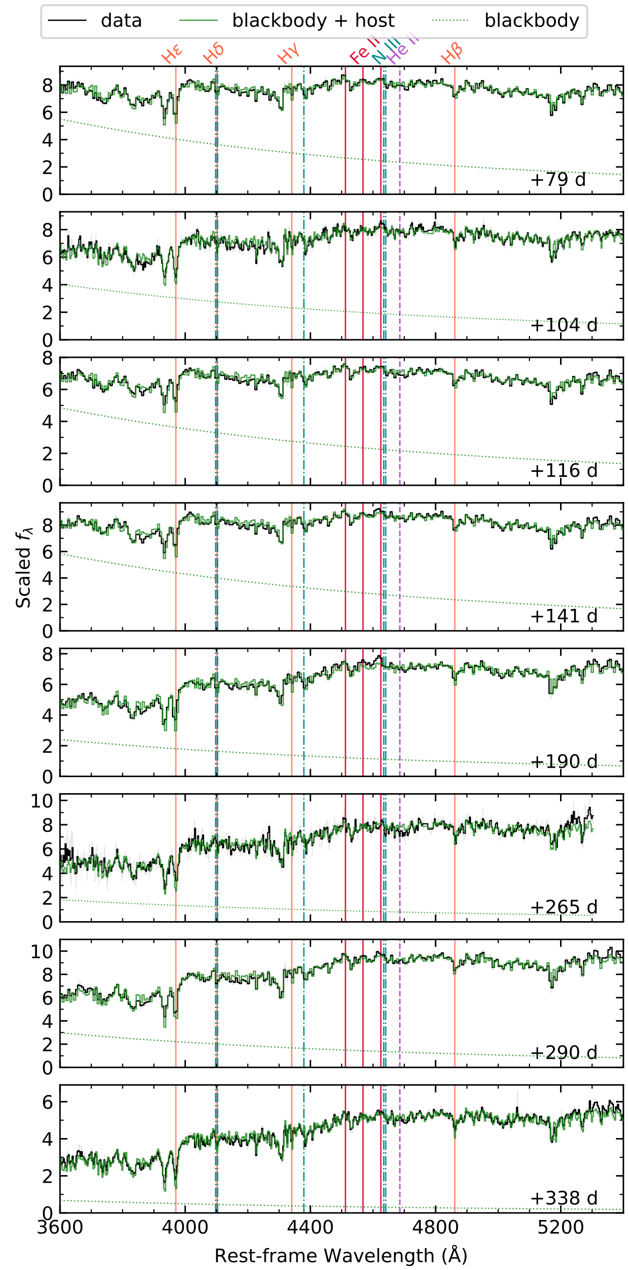

Figure 6. Long-slit optical spectra of AT2021ehb taken at five different epochs. The spectrum ($f_{\lambda,\rm obs}$) is plotted in black. The blackbody continuum ($A_1 f_{\lambda,\rm BB}$; dotted lines) plus host galaxy spectrum ($A_2 f_{\lambda,\rm host}$) is plotted in green. No spectral features commonly seen in optically selected TDEs are observed in AT2021ehb.

While the temperature of AT2021ehb ($T_{\rm bb} \sim 2.5 \times 10^4$ K) is typical among optical and X-ray bright TDEs, its peak radius ($R_{\rm bb} \sim 3 \times 10^{14}$ cm) and luminosity ($L_{\rm bb} \sim 3 \times 10^{43}\,{\rm erg\,s^{-1}}$) are at the low end of the distributions. We note that in the ZTF-I sample of 30 TDEs (Hammerstein et al. 2022), only two objects (AT2020ocn and AT2019wey) have peak radius smaller than that of AT2021ehb (see a discussion in §6.5).

5.2. *Optical Spectral Analysis*

Figure 2 shows that no broad line is evident in the optical spectra of AT2021ehb. To search for weak spectral features from the TDE, we fit the Galactic extinction corrected long-slit spectra in rest-frame 3600–5400 Å using a combination of blackbody emission and host galaxy contribution: $f_{\lambda,\rm obs} = A_1 f_{\lambda,\rm BB} + A_2 f_{\lambda,\rm host}$. Here $f_{\lambda,\rm BB} = \pi B_\lambda(T_{\rm bb})(R^2_{\rm bb}/D^2_L)$, where $T_{\rm bb}$ and $R_{\rm bb}$ are obtained by linear interpolating the blackbody parameters derived in §5.1 at the relevant δt. $f_{\lambda,\rm host}$ is the predicted host galaxy spectrum obtained in §4.2 con-

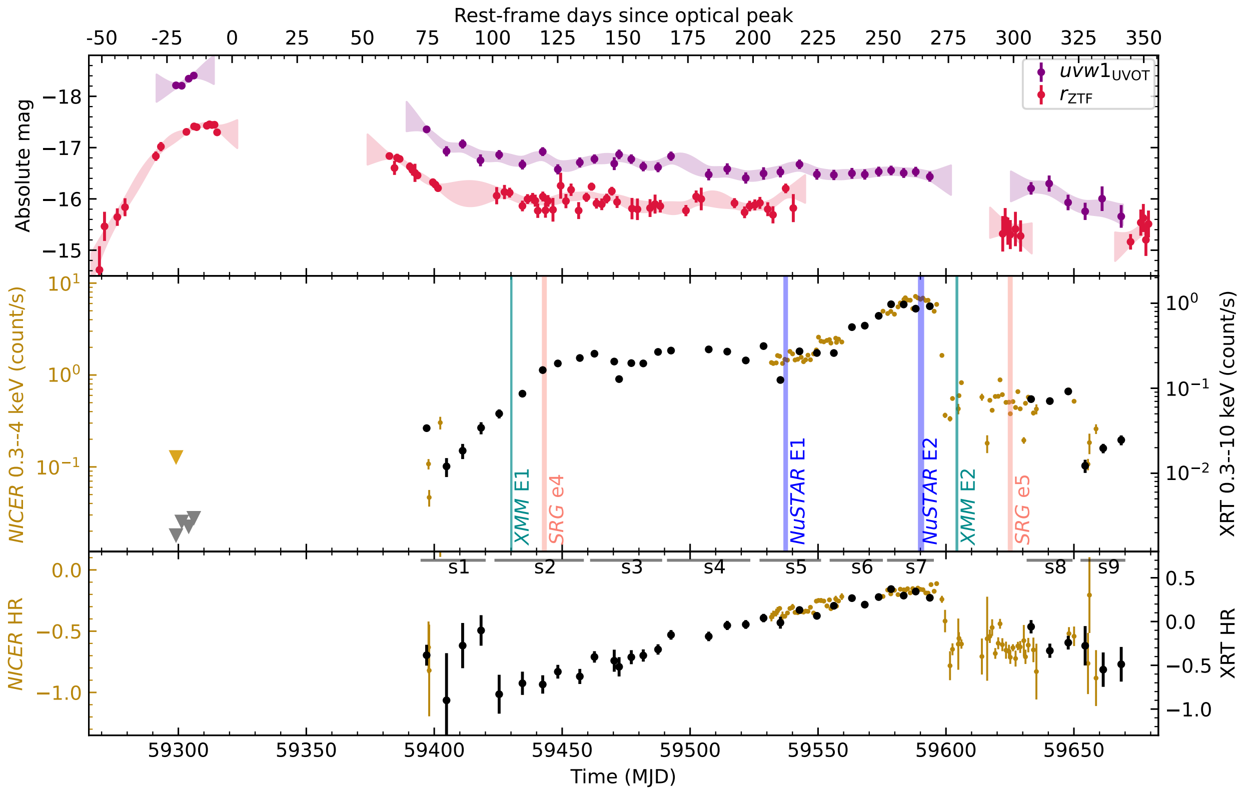

Figure 7. *Upper*: UV ($uvw1_{\rm UVOT}$) and optical ($r_{\rm ZTF}$) light curves of AT2021ehb. *Middle*: XRT and *NICER* X-ray net count rates of AT2021ehb. Epochs of *XMM-Newton*, *SRG*, and *NuSTAR* observations are marked by the vertical lines. *Bottom*: XRT and *NICER* hardness ratio (HR) evolution of AT2021ehb.

volved with the instrumental broadening $\sigma_{\rm inst}$ (see Appendix B). A_1 and A_2 are constants added to account for unknown factors, including the varying amount of host galaxy flux falling within the slit (which depends on the slit width, slit orientation, seeing condition, and target acquisition), uncertainties in the absolute flux calibration and the adopted blackbody parameters. We note that $f_{\lambda,\rm host}$ is the predicted spectrum for the whole galaxy, and therefore might not be a perfect description of the bulge spectrum.

The fitting results are shown in Figure 6. We mark locations of emission lines commonly seen in TDEs, including Balmer lines, He II, the Bowen fluorescence lines of N III and O III, as well as low-ionization Fe II lines (Blanchard et al. 2017; Wevers et al. 2019b). The observed spectra of AT2021ehb can be well described by a blackbody continuum (dotted lines) plus host galaxy contribution. The spectra at $\delta t > 170$ days are mostly host, and therefore it is not very surprising that no discernible TDE lines were detected. However, at $\delta t < 170$ days, the blackbody component contribute 25%–80% of the total flux. As such, it is surprising that no prominent lines from the TDE itself can be identified. We further discuss this result in §6.5.

5.3. *X-ray Light Curve Analysis*

The middle panel of Figure 7 shows the XRT and *NICER* (all binned by obsID) light curves. The bottom panel of Figure 7 shows the evolution of HR, defined as $\mathrm{HR} \equiv (H - S)/(H + S)$, where H is the number of net counts in the hard band, and S is the number of net counts in 0.3–1 keV. For XRT we take 1–10 keV as the hard band, while for *NICER* we take 1–4 keV.

X-rays were not detected at $\delta t < 0$. Pre-peak X-ray upper limits are provided by *Swift*/XRT ($< 10^{40.9}\,{\rm erg\,s^{-1}}$, Table 7) and *SRG*/eROSITA ($< 10^{40.2}\,{\rm erg\,s^{-1}}$, Table 1).

X-rays were first detected by XRT at $\delta t = 73.9$ days. The exact time of the X-ray onset can't be accurately constrained. The count rate initially exhibited strong variability from $\delta t = 73.9$ days to $\delta t = 82.3$ days, and then gradually increased out to $\delta t = 250$ days. At the same time, the HR gradually increased. From $\delta t = 250$ days to $\delta t = 271$ days, both the X-ray flux and the hardness stayed at the maximum values.

From $\delta t = 271.0$ days to $\delta t = 273.7$ days, the *NICER* net count rate suddenly decreased by a factor of 10 (Yao

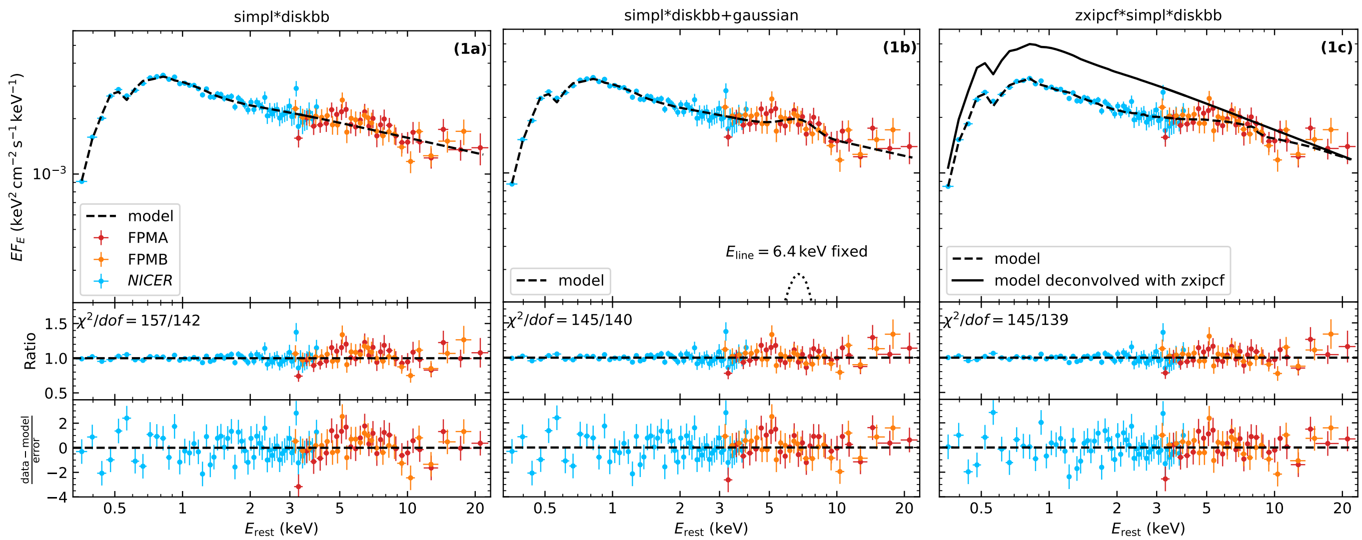

Figure 8. The spectrum of the first joint *NICER* and *NuSTAR* observations (2021 November). See Table 3 for best-fit parameters. FPMB and *NICER* data have divided by $C_{\rm FPMB}$ and $C_{\rm NICER}$, respectively. The data have been rebinned for visual clarity. In the right panel, we also show the best-fit model (1c) deconvolved with the `zxipcf` component.

Table 3. Modeling of the first joint *NICER* and *NuSTAR* observations, $\delta t = 212$ days.

Component	Parameter	(1a)	(1b)	(1c)
`constant`	$C_{\rm FPMB}$	1.03 ± 0.03	1.03 ± 0.03	1.03 ± 0.03
	$C_{\rm NICER}$	$0.86^{+0.04}_{-0.03}$	0.90 ± 0.04	0.92 ± 0.04
`ztbabs`	$N_{\rm H}$ (10^{20} cm^{-2})	< 0.48	< 0.48	$1.78^{+0.71}_{-0.69}$
`simpl`	Γ	2.28 ± 0.03	2.28 ± 0.03	$2.48^{+0.03}_{-0.07}$
	$f_{\rm sc}$	0.28 ± 0.01	$0.28^{+0.02}_{-0.01}$	0.35 ± 0.03
`diskbb`	$T_{\rm in}$ (eV)	169 ± 4	169 ± 4	166 ± 5
	$R^*_{\rm in}$ (10^4 km)	$26.3^{+2.3}_{-1.6}$	$25.8^{+2.3}_{-1.6}$	$33.1^{+7.0}_{-4.1}$
`gaussian`	$E_{\rm line}$ (keV)	...	6.4 (fixed)	...
	$\sigma_{\rm line}$) (keV)	...	1.20 ± 0.33	...
	Norm (10^{-5} ph cm^{-2} s^{-1})	...	$2.09^{+0.75}_{-0.69}$	...
`zxipcf`	$N_{\rm H}$ (10^{22} cm^{-2})	...	...	15 (fixed)
	$\log\xi$	...	...	$1.97^{+0.07}_{-0.04}$
	$f_{\rm cover}$	...	...	$0.41^{+0.07}_{-0.09}$
	Redshift	...	...	-0.16 ± 0.04
—	χ^2/dof	157.11/142	145.48/140	144.75/139

et al. 2022). At the same time, the HR significantly decreased. After an X-ray plateau of ≈ 50 days, the XRT net count rate further decreased drastically by a factor of 6 (from $\delta t = 320.9$ days to $\delta t = 327.2$ days).

5.4. *X-ray Spectral Analysis*

In this subsection, we first present joint spectral analysis of contemporaneous data sets obtained from *NICER* and *NuSTAR*, including the first epoch in 2021 November 18–19 (§5.4.1) and the second epoch in 2022 January 10–12 (§5.4.2). These observations are of high signal-to-noise ratio (SNR) and cover a wide energy range. As such, the fitting results can guide us to choose appropriate spectral models to fit spectra with lower SNR. We then perform analysis on data sets obtained by single telescopes, including *XMM-Newton* (§5.4.3), *SRG* (§5.4.4), *Swift*/XRT (§5.4.5), and *NICER* (§5.4.6).

All spectral fitting were performed with `xspec` (v12.12, Arnaud 1996). We used the `angr` abundances

(Anders & Grevesse 1989) and the vern cross sections (Verner et al. 1996).

5.4.1. *NICER+NuSTAR First Epoch, 2021 November*

We chose energy ranges where the source spectrum dominates over the background. For *NICER* we used 0.3–4 keV. For FPMA we used 3–23 keV, for FPMB we used 3–20 keV[7]. All data were fitted using χ^2-statistics.

For all spectral models described below, we included the Galactic absorption using the tbabs model (Wilms et al. 2000), with the hydrogen-equivalent column density $N_{\rm H}$ fixed at $9.97 \times 10^{20}\,{\rm cm}^{-2}$ (HI4PI Collaboration et al. 2016). We shifted the TDE emission using the convolution model zashift, with the redshift z fixed at 0.018. We included possible absorption intrinsic to the source using the ztbabs model. We also included a calibration coefficient (constant; Madsen et al. 2017) between FPMA, FPMB, and *NICER*, with $C_{\rm FPMA} \equiv 1$.

First, we fitted the spectrum with a power-law (PL), and obtained a photon index of $\Gamma \approx 2.7$. The fit is unacceptable, with the reduced χ^2 value being $\chi^2_{\rm r} = 3.44$ for a degrees of freedom (dof) of 144. The residual is most significant at 0.3–2 keV, suggesting the existence of a (thermal) soft component. Therefore, we changed the PL to simpl*thermal_model. Here simpl is a Comptonization model that generates the PL component via Compton scattering of a fraction ($f_{\rm sc}$) of input seed photons (Steiner et al. 2009). The flag $R_{\rm up}$ was set to 1 to only include upscattering. We experimented with three different thermal models: a blackbody (bbody), a multicolor disk (MCD; diskbb; Mitsuda et al. 1984), and a single-temperature thermal plasma (bremss; Kellogg et al. 1975), resulting in $\chi^2_{\rm r} = 1.29$, 1.11, and 1.31 (for $dof = 142$), respectively. The fit statistics favors a MCD.

The best-fit result with a MCD, defined as model (1a), is shown in the left panel of Figure 8. We present the best-fit parameters in Table 3. Here $T_{\rm in}$ is the inner disk temperature, and $R^*_{\rm in} \equiv R_{\rm in}\sqrt{\cos i}$ is the apparent inner disk radius times square root of $\cos i$, where i is the system inclination. $R^*_{\rm in}$ is inferred from the normalization parameter of diskbb. Model (1a) gives a good fit with $\chi^2_{\rm r} = 157/142 = 1.11$. However, a flux excess between 5 keV and 8 keV can been seen in the residual plot. As such, we tried two more complex models.

In model (1b), we added a gaussian component with the line center $E_{\rm line}$ fixed at 6.4 keV, where the normalization and line width ($\sigma_{\rm line}$) were allowed to be free. This is motivated by the weak 5–8 keV flux excess of model (1a). The best-fit model, with $\chi^2_{\rm r} = 1.04$, is shown in the middle panel of Figure 8.

[7] In this *NuSTAR* observation, FPMB is more affected by a nearby bright source.

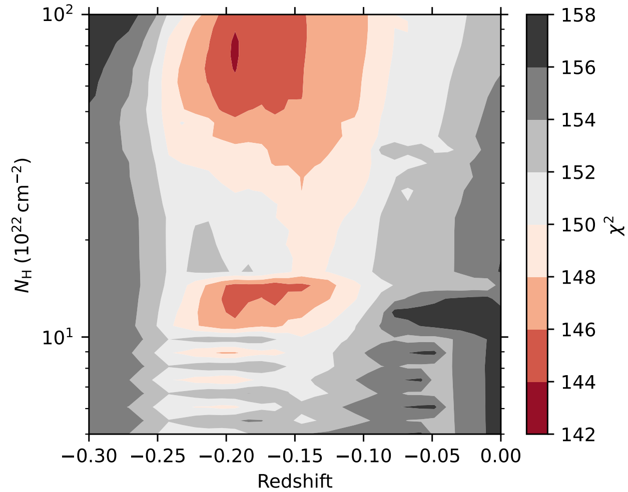

Figure 9. The χ^2 values of model (1c) as a function of two parameters ($N_{\rm H}$ and redshift) in the zxipcf component. This contour shows that the fitting is insensitive to $N_{\rm H}$.

In model (1c), motivated by the possible detection of a sub-relativistic outflow in the *Chandra* LETG observation conducted on 2021 November 29 (Miller et al. 2022), we added partial-covering absorption by convolving the continuum with a zxipcf model (Reeves et al. 2008). zxipcf calculates X-ray absorption using a grid of photoionization models computed by the XSTAR code (Kallman & Bautista 2001). It has four free parameters for the absorbing material: the hydrogen-equivalent column density $N_{\rm H}$, the redshift, the fraction over which it covers the X-ray source $f_{\rm cover}$, and the ionization parameter $\log\xi \equiv L_{\rm ion}/(nr^2)$ (Tarter et al. 1969). Here $L_{\rm ion}/r^2$ is the local source ionizing flux integrated between 1 and 1000 Rydberg, and n is the hydrogen number density.

First, we allowed all four parameters of zxipcf to be free, and ran the steppar command to examine the fit statistics on the 2-dimensional (2D) grids between any two parameters. We found that when the column density $N_{\rm H}$ of the absorbing material was varied, the distribution of χ^2 would show more than one minimum (see an example in Figure 9). Therefore, we then fixed $N_{\rm H}$ at $15 \times 10^{22}\,{\rm cm}^{-2}$, and allow other parameters to be free. The fitting result, with $\chi^2_{\rm r} = 1.04$, is shown in the right panel of Figure 8.

Table 3 presents the best-fit parameters and fit statistics. Compared with (1a), both (1b) and (1c) improved the fit. From a spectral modeling point of view, we are not able to tell whether the data favors (1b) or (1c).

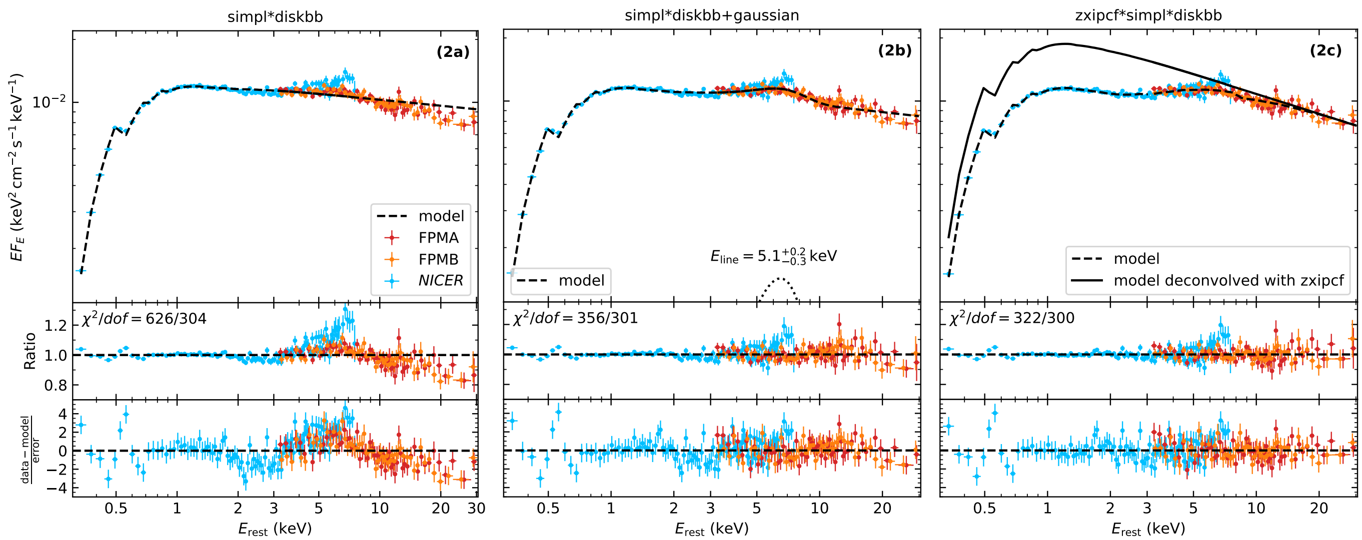

Figure 10. The spectrum of the second joint *NICER* and *NuSTAR* observations (2022 January). See Table 4 for best-fit parameters. FPMB and *NICER* data have divided by $C_{\rm FPMB}$ and $C_{\rm NICER}$, respectively. The data have been rebinned for visual clarity. In the right panel, we also show the best-fit model (2c) deconvolved with the `zxipcf` component.

However, since adding a `zxipcf` component works best for the second epoch of joint *NICER*+*NuSTAR* observation (see §5.4.2), the 5–8 keV residual seen in model (1a) is more likely to be caused by strong absorption features above 8 keV (from highly ionized iron) and below 5 keV (from low-Z elements), instead of an emission feature in the iron K band. Moreover, the redshift in the `zxipcf` component of model (1c) corresponds to a velocity of $-0.17\pm0.05c$. This is close to the outflow velocity of $-0.15 \pm 0.02c$ measured by *Chandra* grating spectroscopy only 10 days after our first *NICER*+*NuSTAR* observation (Miller et al. 2022). Therefore, we consider model (1c) to be better than (1b).

5.4.2. *NICER+NuSTAR Second Epoch, 2022 January*

We chose energy ranges where the source spectrum dominates over the background. For *NICER* we used 0.3–7.5 keV; For *NuSTAR* FPMA and FPMB we used 3–30 keV. All data were fitted using χ^2-statistics. Unlike in §5.4.1, here we use `tbfeo` to model the Galactic absorption. Compared with `tbabs`, `tbfeo` allows the O and Fe abundances ($A_{\rm O}$, $A_{\rm Fe}$) to be free.

We first adopted a continuum model of `simpl*diskbb`, defined as (2a). The result, with $\chi^2_{\rm r} = 2.06$, is shown in the left panel of Figure 10. The residual plot clearly demonstrates the existence of unmodeled spectral features. Similar to §5.4.1, we attempted to improve the fit by two approaches. In model (2b), we added a `gaussian` component, with the line center, line width, and normalization parameters to be free. In model (2c), we multiplied the continuum by `zxipcf`. The results are shown in the middle and right panels of Figure 10. Table 4 presents the best-fit parameters and fit statistics.

Compared with (2a), the $\chi^2_{\rm r}$ value of (2b) has decreased to 1.18. However, there are still unmodeled spectral features in the residual. Moreover, the best-fit line center of $E_{\rm line} = 5.11^{+0.21}_{-0.27}$ keV is too low to be explained by iron line fluorescence. The iron line profile observed in AGNs and XRBs typically exhibits a distorted red wing (Fabian 2016), while the emission line of model (2b) is very broad and more symmetric. Therefore, we do not consider (2b) as an appropriate description of the data.

Model (2c) provides a good fit with $\chi^2_{\rm r} = 1.07$. The best-fit redshift in the `zxipcf` component corresponds to a velocity of $-0.11 \pm 0.02c$, which is slightly lower than the UFO velocity inferred in model (1c). We note that the residual below 0.8 keV is strong in all model fits, and is likely caused by underestimated *NICER* calibration uncertainties at the lowest energies.

5.4.3. *XMM-Newton Analysis*

We chose energy ranges where the source spectrum dominates over the background. For XMM E1 this is 0.2–2.6 keV, while for XMM E2 this is 0.2–7.0 keV. All data were fitted using χ^2-statistics. Following §5.4.1 and §5.4.2, all models described below have been multiplied by `tbabs*ztbabs*zashift` to include Galactic absorption, host absorption, and host redshift.

Although the XMM E1 spectrum is very soft, a single MCD results in a poor fitting and leaves a large residual above 1 keV, suggesting the existence of a non-thermal

Table 4. Modeling of the second joint *NICER* and *NuSTAR* observations, $\delta t =$ 264 days.

Component	Parameter	(2a)	(2b)	(2c)
`constant`	$C_{\rm FPMB}$	1.03	1.03 ± 0.01	1.03 ± 0.01
	$C_{\rm NICER}$	0.99	1.02 ± 0.01	1.03 ± 0.01
`tbfeo`	$A_{\rm O}$	0.93	0.96 ± 0.03	0.93 ± 0.03
	$A_{\rm Fe}$	1.29	$1.29^{+0.31}_{-0.20}$	$1.50^{+0.19}_{-0.15}$
`ztbabs`	$N_{\rm H}$ (10^{20} cm^{-2})	0.00	< 0.02	< 0.07
`diskbb`	$T_{\rm in}$ (eV)	186	191^{+4}_{-2}	170^{+7}_{-2}
	$R^*_{\rm in}$ (10^4 km)	33.8	$31.7^{+0.9}_{-1.3}$	47.3 ± 2.8
`simpl`	Γ	2.10	2.11 ± 0.01	2.30 ± 0.01
	$f_{\rm sc}$	0.47	0.46 ± 0.01	0.61 ± 0.01
`gaussian`	$E_{\rm line}$ (keV)	...	$5.11^{+0.21}_{-0.27}$	...
	$\sigma_{\rm line}$) (keV)	...	$2.10^{+0.23}_{-0.19}$	...
	Norm (10^{-4} ph cm^{-2} s^{-1})	...	$2.30^{+0.36}_{-0.28}$	...
`zxipcf`	$N_{\rm H}$ (10^{22} cm^{-2})	...	...	$7.67^{+0.50}_{-0.52}$
	$\log\xi$	...	...	$0.60^{+0.30}_{-0.29}$
	$f_{\rm cover}$	...	...	0.35 ± 0.01
	Redshift	...	...	-0.10 ± 0.02
—	χ^2/dof	626.45/304	356.24/301	322.14/300

Note—Parameter uncertainties of model (2a) cannot be calculated since $\chi^2_{\rm r} > 2$.

Table 5. Modeling of two *XMM-Newton* observations.

Component	Parameter	XMM E1		XMM E2	
		(3a)	(3c)	(4a)	(4c)
`ztbabs`	$N_{\rm H}$ (10^{20} cm^{-2})	1.09 ± 0.15	$1.87^{+0.90}_{-0.55}$	< 0.66	$1.71^{+0.75}_{-0.69}$
`diskbb`	$T_{\rm in}$ (eV)	$67.6^{+0.8}_{-3.2}$	$71.5^{+3.3}_{-3.7}$	125 ± 5	110^{+6}_{-7}
	$R^*_{\rm in}$ (10^4 km)	511^{+129}_{-2}	515^{+139}_{-61}	39^{+6}_{-4}	118^{+48}_{-17}
`simpl`	Γ	> 4.70 (upper limit at 5)	$3.87^{+0.22}_{-0.21}$	2.92 ± 0.09	$3.39^{+0.14}_{-0.16}$
	$f_{\rm sc}$	$0.126^{+0.023}_{-0.004}$	$0.070^{+0.016}_{-0.010}$	$0.163^{+0.019}_{-0.016}$	$0.26^{+0.06}_{-0.04}$
`zxipcf`	$N_{\rm H}$ (10^{22} cm^{-2})	...	$93.4^{+29.2}_{-23.8}$	...	$7.6^{+8.8}_{-0.9}$
	$\log\xi$	...	$3.07^{+0.08}_{-0.07}$	...	< -0.23 (lower limit at -3)
	$f_{\rm cover}$	...	> 0.94	...	$0.78^{+0.04}_{-0.05}$
	Redshift	...	$-0.256^{+0.023}_{-0.014}$	...	0 (fixed)
—	χ^2/dof	70.26/52	42.14/48	97.49/82	72.97/79

component. A continuum model of `simpl*diskbb` gives a much better fit with $\chi^2_{\rm r} = 1.35$. The best-fit model,x named as (3a), is shown in the left panel of Figure 11. Some residual can be seen at 0.8–1.7 keV.

Following §5.4.1 and §5.4.2, we then added absorption from a partially ionized outflow using `zxipcf`. The right panel of Figure 11 shows that the new model, named as (3c), gives a better description of the data. The best-fit redshift parameter (Tabel 5) corresponds to a velocity of $v = -0.29^{+0.03}_{-0.02}$c, which is greater than the UFO velocities found by our joint *NICER*+*NuSTAR* observations.

The XMM E2 spectrum is much harder than XMM E1. Fitting with `simpl*diskbb` gives a good fit with $\chi^2_{\rm r} =$ 1.19 (see Figure 12, left panel). To be consistent with the XMM E1 analysis, we also fitted XMM E2 with `zxipcf*simpl*diskbb`, leading to a lower $\chi^2_{\rm r}$. However,

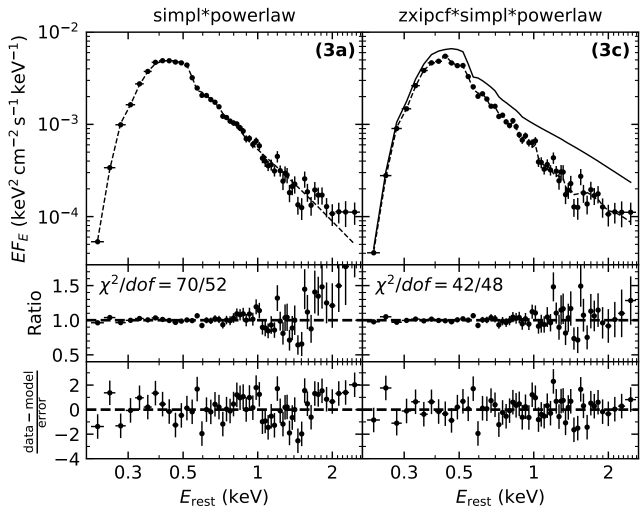

Figure 11. The XMM E1 spectrum. The dashed lines show the best-fit models. The solid line shows model (3c) deconvolved with the `zxipcf` component. See Table 5 for the best-fit parameters.

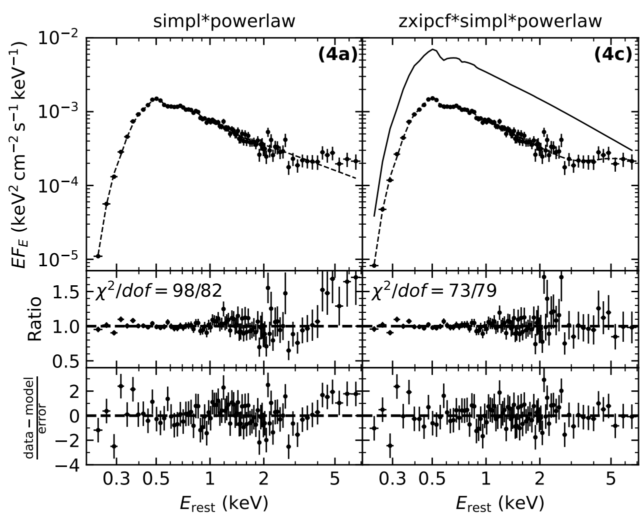

Figure 12. The XMM E2 spectrum. The dashed lines show the best-fit models. The solid line shows model (3c) deconvolved with the `zxipcf` component. See Table 5 for the best-fit parameters.

we found that there exists a strong degeneracy between the $N_{\rm H}$ and redshift parameters in the `zxipcf` component (see Figure 13). Therefore, we then fixed the outflow redshift at 0, and allowed other parameters to be free. The result, shown in the right panel of Figure 12, mainly improves the fit at 2.5–7 keV.

The complete list of model parameters is presented in Table 5. Since the $\chi^2_{\rm r}$ values of (3c) and (4c) are all smaller than 1, we also use the Bayesian information

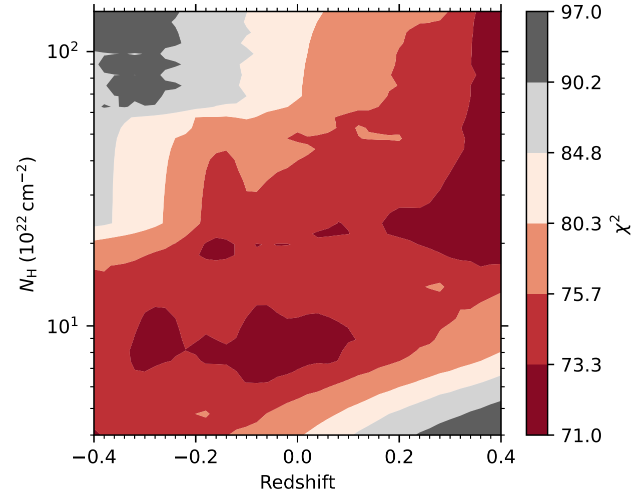

Figure 13. The χ^2 values of model (4c) as a function of two parameters in the `zxipcf` component. This contour shows that there is a strong degeneracy between $N_{\rm H}$ and redshift.

criterion (BIC) to assess the goodness of fit. Here

$$\mathrm{BIC} = k \cdot \ln(N) - 2\ln\mathcal{L} \quad (1)$$
$$= k \cdot \ln(N) + \chi^2 + \text{constant} \quad (2)$$

where k is the number of free parameters, N is the number of spectral bins, and $\mathcal{L}$ is the maximum of the likelihood function. Models with lower BIC values are favored. We have BIC(3c) − BIC(3a) = −11.9, and BIC(4c) − BIC(4a) = −11.3, supporting the presence of absorption from ionized materials in both XMM E1 and XMM E2.

5.4.4. *SRG/eROSITA Analysis*

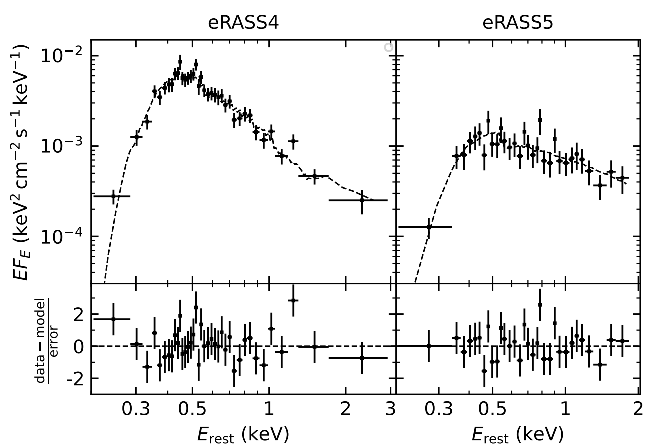

Figure 14. *SRG*/eROSITA spectra of AT2021ehb.

We chose energy ranges where the source spectrum dominates over the background. For eRASS4 this range is 0.2–3 keV, while for eRASS5 this range is 0.2–2 keV. All data were fitted with C-statistic.

Following §5.4.1, §5.4.2, and §5.4.3, we fitted the *SRG*/eROSITA spectra with `tbabs*ztbabs*zashift*zxipcf*simpl*diskbb`. Since the eROSITA spectra are of lower SNR, we are not able to simultaneously constrain all model parameters. Therefore, for eRASS4 and eRASS5, we fixed the four parameters in the `zxipcf` component using the best-fit values of model (3c) and (4c) (Table 5), respectively. This is because the eRASS4 observation was conducted at a time close to XMM E1, and the eRASS5 observation was conducted at a time close to XMM E2 (see Figure 7). For the eRASS5 observation, we also found that the fit was insensitive to the normalization parameter of `diskbb`. Therefore, we also fixed this parameter at the best-fit value of model (4c).

The fitting results are shown in Figure 14. For the eRASS4 spectrum, we obtained host $N_{\rm H} < 1.5 \times 10^{20}\,{\rm cm^{-2}}$, $T_{\rm in} = 87 \pm 9\,{\rm eV}$, $R^*_{\rm in} = 276^{+130}_{-57} \times 10^4\,{\rm km}$, $\Gamma = 3.48^{+0.42}_{-0.44}$, $f_{\rm sc} = 0.12^{+0.07}_{-0.04}$, and $cstat/dof = 124/140$. For the eRASS5 spectrum, we obtained host $N_{\rm H} < 0.9 \times 10^{20}\,{\rm cm^{-2}}$, $T_{\rm in} = 105 \pm 4\,{\rm eV}$, $\Gamma = 3.04 \pm 0.32$, $f_{\rm sc} = 0.19 \pm 0.10$, and $cstat/dof = 75/85$.

5.4.5. *XRT Analysis*

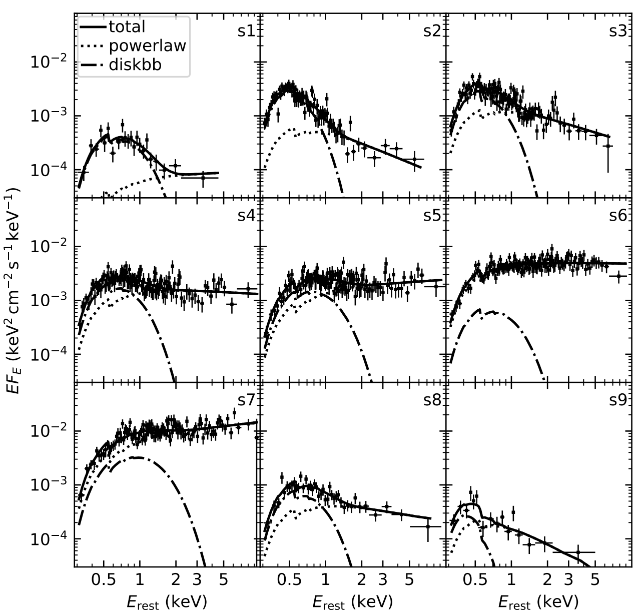

Figure 15. XRT time-averaged spectra of AT2021ehb. See the bottom panel of Figure 7 for the time span of each spectrum.

The temporal coverage of each time-averaged XRT spectrum (generated in §3.4.1) is shown as ‘s1’, ‘s2’, ..., ‘s9’ in the bottom panel of Figure 7. Given that the high SNR observations favor the addition of a `zxipcf` component (see §5.4.1, §5.4.2, and §5.4.3), absorption from ionized materials are probably also present in the XRT data. However, the XRT data are of lower SNR, making it difficult to constrain many free parameters.

Therefore, we fitted the 0.3–10 keV spectra using a simple model of `tbabs*zashift*(diskbb+powerlaw)`. We did not include the `ztbabs` component as host galaxy absorption was found to be negligable or much smaller than the Galactic absorption in all previous spectral analysis (see Table 3, Table 4, Table 5, and §5.4.4). The adopted continuum model does not give realistic model parameters. For example, the disk radii would be underestimated when the source spectra are hard (see a detailed discussion in Steiner et al. 2009). The main goal of this fitting is to compute the multiplicative factor to convert the 0.3–10 keV XRT net count rate to the 0.3–10 keV flux (both observed and Galactic absorption corrected), as well as the Galactic absorption corrected 0.5–10 keV flux and the flux density at the rest-frame energy of 0.5 keV and 2 keV, which will later be used in §5.5. All data were fitted using C-statistics.

The best-fit models are shown in Figure 15. Appendix A.2 (Table 8) provides the scaling factors to convert 0.3–10 keV net count rate to X-ray fluxes. The observed isotropic equivalent 0.3–10 keV X-ray luminosity, $L_{\rm X}$, is shown in the upper panel of Figure 16. Note that for the initial four XRT non detections, we assume a spectral shape similar to ‘s1’.

5.4.6. *NICER Analysis*

We started with the obsID-binned *NICER* spectra generated in §3.5. We only performed spectral fitting on obsIDs with more than 500 total net counts in 0.3–4 keV. Following §5.4.5, we fitted a `tbabs*zashift*(diskbb+powerlaw)` model to the 0.3–4 keV spectra and inferred $f_{\rm X}$ from the best-fit models. All data were fitted using χ^2-statistics. The best-fit models provided a $\chi^2_{\rm r}$ close to 1 in most of the cases. The $L_{\rm X}$ evolution inferred from *NICER* spectral fitting is also shown in the upper panel of Figure 16.

5.5. *Spectral Indices* $\alpha_{\rm OX}$ *and* $\alpha_{\rm OSX}$

To assist comparison with literature TDEs, we computed the UV to X-ray spectral index $\alpha_{\rm OX}$ (Tananbaum et al. 1979; Ruan et al. 2019; Wevers et al. 2021) and $\alpha_{\rm OSX}$ (Gezari 2021), which are commonly used in AGN and TDE literature to characterize the ratio of UV to

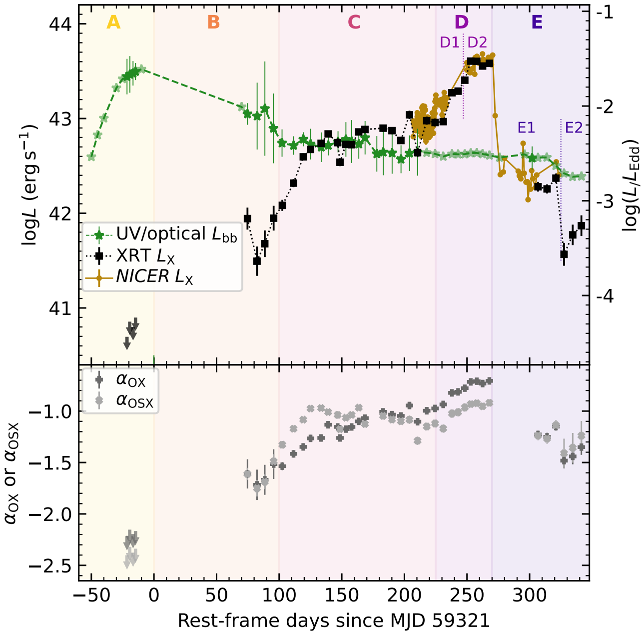

Figure 16. *Upper*: Blackbody luminosity of the UV/optical emission ($L_{\rm bb}$; §5.1) compared with the observed isotropic equivalent 0.3–10 keV X-ray luminosity (L_X) from XRT (§5.4.5) and *NICER* (§5.4.6). *Bottom*: the 2500 Å to X-ray spectral slope measured by *Swift* observations (Eq. 3, 4).

X-ray fluxes[8]. Here

$$\alpha_{\rm OX} \equiv \frac{\log[L_\nu(2500\,\text{Å})/L_\nu(2\,\text{keV})]}{\log[\nu(2500\,\text{Å})/\nu(2\,\text{keV})]}, \tag{3}$$

$$\alpha_{\rm OSX} \equiv \frac{\log[L_\nu(2500\,\text{Å})/L_\nu(0.5\,\text{keV})]}{\log[\nu(2500\,\text{Å})/\nu(0.5\,\text{keV})]}, \tag{4}$$

where L_ν is the luminosity at a certain frequency (corrected for $N_{\rm H}$ and $E_{B-V,\rm MW}$). We use the *Swift uvw*1 host-subtracted luminosities (rest-frame effective wavelength at 2459 Å for $T_{\rm eff} = 3\times10^4$ K) as a proxy for $L_\nu(2500\,\text{Å})$. We measure $f_\nu(0.5\,\text{keV})$ and $f_\nu(2\,\text{keV})$ by converting the XRT net count rates to flux densities using the scaling factors derived in §5.4.5. We note that $f_\nu(2\,\text{keV})$ mainly traces the evolution of the non-thermal X-ray component, while $f_\nu(0.5\,\text{keV})$ traces both the thermal and non-thermal components. The results are shown in the bottom panel of Figure 16.

Based on Figure 16, we divide the evolution of AT2021ehb into five phases. In phase A ($\delta t \lesssim 0$ days), the UV/optical luminosity brightens, while X-rays are not detected at $< 10^{40.9}\,{\rm erg\,s^{-1}}$. In phase B ($0 \lesssim \delta t \lesssim 100$ days), the UV/optical luminosity decays, and X-rays emerge. Entering into phase C ($100 \lesssim \delta t \lesssim 225$ days), the X-ray spectrum gradually hardens, while the UV/optical luminosity stays relatively flat. In phase D ($225 \lesssim \delta t \lesssim 270$ days), the X-ray further brightens for two times (indicated by D1 and D2), and the UV/optical plateau persists. In phase E, the X-ray luminosity drops for two times (indicated by E1 and E2), while the UV/optical luminosity only slightly declines. Interestingly, the dramatic X-ray evolution in phase D+E does not have much effect on the UV/optical luminosity. Typical SEDs in each phase are shown in Figure 17.

[8] Note that some papers use these indices with a minus sign in front of our definitions.

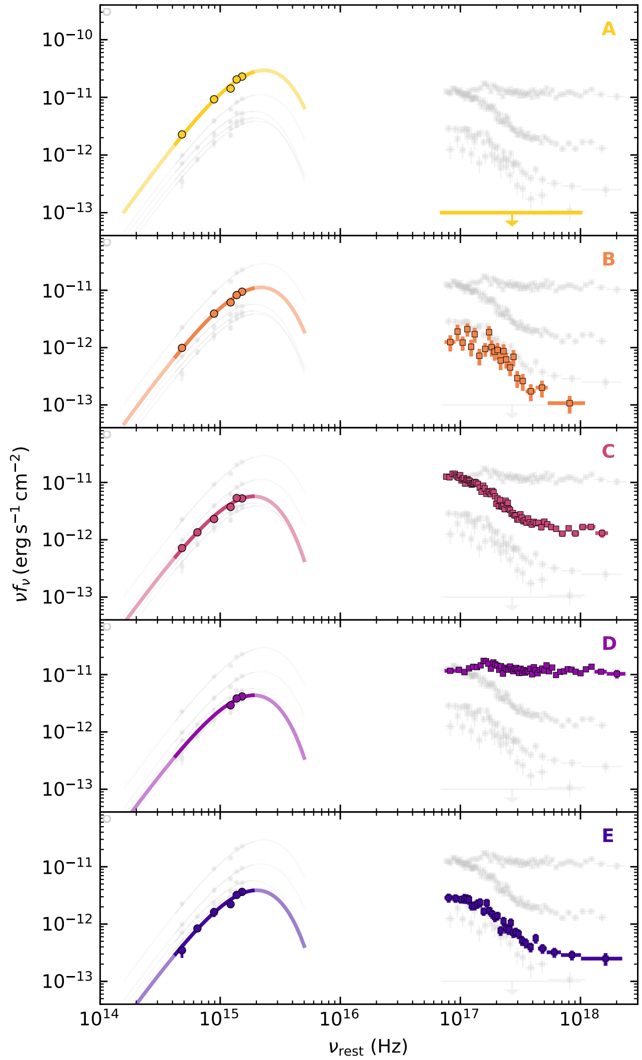

Figure 17. Typical SEDs of AT2021ehb in five phases. The data has been corrected for extinction (in UV/optical) and column density absorption (in the X-ray). The solid lines are the blackbody fits to UV/optical data.

5.6. *Bolometric Luminosity $L_{\rm bol}$*

To calculate the bolometric luminosity $L_{\rm bol}$ at epochs of *Swift* observations, we assume that the bulk of radiation between 10000 Å and 10 keV. We estimate that when the X-ray spectrum is the hardest (i.e., model 2c), the 0.3–10 keV flux still constitutes 72% of the 0.3–100 keV flux. Therefore, this assumption at most underestimates $\log L_{\rm bol}$ by 0.14 dex.

We compute the 10000 Å to 10 keV luminsoity by adding the luminosities in three energy ranges (see a demonstration in Figure 18).

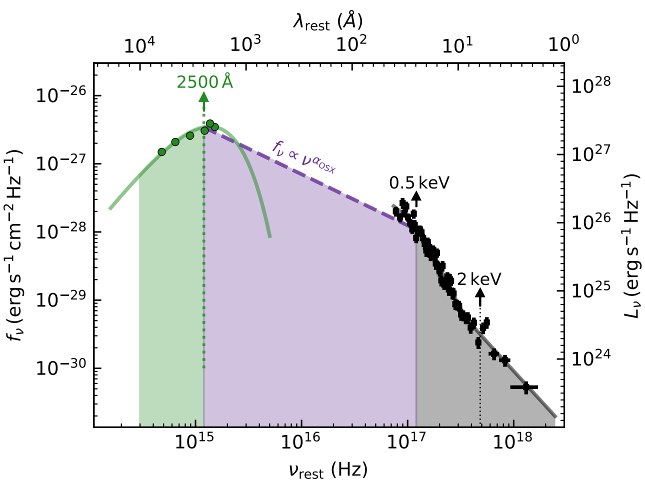

Figure 18. A snapshot SED of AT2021ehb at $\delta t \approx 147$ days. The data has been corrected for extinction (in UV/optical) and Galactic absorption (in the X-ray). The solid lines are the blackbody fits to UV/optical data (§5.1) and the XRT 's3' spectrum best-fit model (§5.4.5). The shaded region shows that the $L_{\rm bol}$ is calculated in three energy ranges (see text).

From 10000 Å to 2500 Å, we integrate below the blackbody model fitted to the UV/optical photometry (§5.1).

From 2500 Å to 0.5 keV, we assume that the TDE spectrum is continuous and can be approximated by a power-law of $f_\nu \propto \nu^{\alpha_{\rm OSX}}$. This assumption has the advantage of being model independent, and is motivated by both analytical studies of relativistic thin disks (see Fig. 5 of Mummery & Balbus 2020) and general relativistic radiation magnetohydrodynamics (GRRMHD) simulations of super-Eddington thick disks (see Fig. 5 of Dai et al. 2018 and Fig. 12 of Curd & Narayan 2019). Hence, the luminosity is

$$L = \int_{\nu_1}^{\nu_2} L_\nu d\nu \approx \int_{\nu_1}^{\nu_2} \frac{L_\nu(\nu_1)}{\nu_1^{\alpha_{\rm OSX}}} \nu^{\alpha_{\rm OSX}} d\nu \tag{5}$$

$$= \frac{L_\nu(\nu_1)}{\nu_1^{\alpha_{\rm OSX}}} \times \begin{cases} \dfrac{\nu_2^{\alpha_{\rm OSX}+1} - \nu_1^{\alpha_{\rm OSX}+1}}{\alpha_{\rm OSX}+1} & \text{if } \alpha_{\rm OSX} \neq -1 \\ \ln(\nu_2/\nu_1) & \text{if } \alpha_{\rm OSX} = -1 \end{cases} \tag{6}$$

where $\nu_1 = 10^{15.08}$ Hz, $\nu_2 = 10^{17.08}$ Hz. In this range, we assume that the uncertainty of L is $0.3L$.

From 0.5 keV to 10 keV, we calculate the luminosity by converting the 0.3–10 keV XRT net count rate to Galactic absorption corrected 0.5–10 keV luminosity using the scaling factors derived in §5.4.5.

Note that for the first four *Swift* epochs, since X-rays were not detected, we use the UV/optical blackbody luminosity $L_{\rm bb}$ as an approximation of $L_{\rm bol}$.

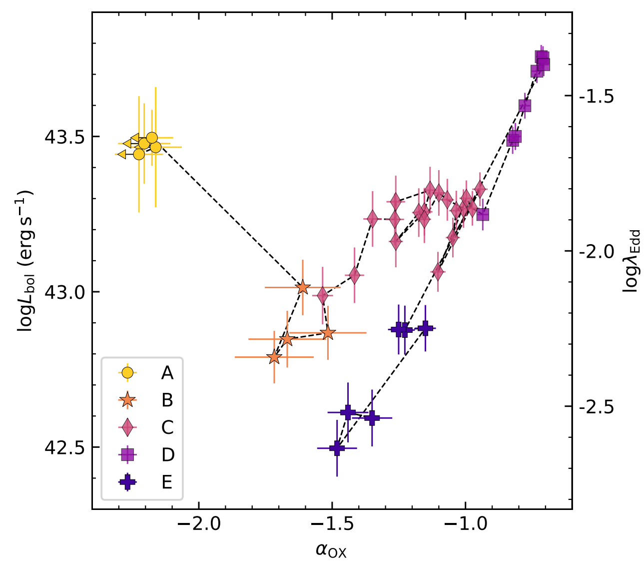

Figure 19. The bolometric luminosity $L_{\rm bol}$ as a function of $\alpha_{\rm OX}$. Note that the uncertainty of $\lambda_{\rm Edd}$ is greater than the uncertainty of $L_{\rm bol}$ by 0.44 dex (i.e., the uncertainty of $M_{\rm BH}$; §4.1), which is not included in the figure.

The evolution of $\log L_{\rm bol}$ as a function of $\alpha_{\rm OX}$ is shown in Figure 19. The data points are color coded by their phases (from A to E, see Figure 16). The right y-axis converts $L_{\rm bol}$ to the Eddington ratio $\lambda_{\rm Edd} \equiv L_{\rm bol}/L_{\rm Edd}$. For pure hydrogen, a $M_{\rm BH}$ of $10^{7.03}\,M_\odot$ (§4) implies an Eddington luminosity of $L_{\rm Edd} \approx 10^{45.13}\,{\rm erg\,s^{-1}}$. We further discuss this figure in §6.4.

6. DISCUSSION

Hereafter we define $M_7 \equiv M_{\rm BH}/(10^7\,M_\odot)$, $\dot{m} \equiv \dot{M}_{\rm acc}/\dot{M}_{\rm Edd}$, $\dot{M}_{\rm Edd} \equiv L_{\rm Edd}/(\eta c^2)$, $\eta_{-1} \equiv \eta/10^{-1}$, where $\dot{M}_{\rm acc}$ is the mass accretion rate and η is the accretion radiative efficiency. With $M_7 \approx 1$, the gravitational radius is $R_{\rm g} = GM_{\rm BH}/c^2 \approx 10^{12.20}$ cm. For a solar type star, the tidal radius is $R_{\rm T} = 10^{13.19}\,{\rm cm} \approx 10 R_{\rm g}$.

6.1. *Detection and Evolution of an UFO*

A main result of this work is that an ionized UFO that can be modeled with `zxipcf` is present not only in the two epochs of *NICER*+*NuSTAR* observations (§5.4.1,

§5.4.2), but also in the two *XMM-Newton* observations (§5.4.3). We show the evolution of relevant outflow parameters in the bottom four panels of Figure 20. Interestingly, in phase C–D, the outflow velocity is higher (more negative) at earlier times, when the X-ray spectrum is softer.

Moreover, in phase C–D, the hydrogen-equivalent column $[N_{\rm H} = \int n(r)dr]$ along the line-of-sight and the ionization parameter of the UFO generally decrease from early to late time. If the UFO has a spherical density profile of $n \propto r^{-\alpha}$, then the observed trend of $N_{\rm H}$ suggests a steep density profile with $\alpha \sim 3$. However, this will lead to $\xi = L_{\rm ion}/(nr^2) \propto r$, which is not consistent with the observed trend of decreasing logξ. Therefore, we infer that either the UFO does not have a steady spherical structure or/and the ionizing luminosity has significantly dropped at later times.

If the UFO is launched from the accretion disk, the minimum wind launching radius corresponds to the radius where the observed velocity equals to the escape velocity of $r = 2GM_{\rm BH}/v^2$. At $0.3c$ and $0.1c$, the radii are $22R_{\rm g}$ and $200R_{\rm g}$. This would require the disk outer radius to extend beyond $20R_{\rm T}$, which is much greater than the expected TDE circularization radius predicted by numerical simulations (Bonnerot et al. 2016, 2021).

Alternatively, the UFO can be generated by a self-crossing shock (Jiang et al. 2016; Lu & Bonnerot 2020). Its self-intersection radius is determined by the amount of general relativistic apsidal precession as given by the pericenter of the initial star's orbit (Dai et al. 2015). Therefore, we expect the power of the self-crossing shock to track the fallback rate and decay with time as $\sim t^{-5/3}$ (Rees 1988; Phinney 1989), which can explain the smaller UFO velocity and column density at later times.

Compared with a disk-driven outflow, a collisional-induced outflow (CIO) is also expected to be much denser near the self-crossing point and is hence more capable of reprocessing the hard emission from the disk (Bonnerot et al. 2021). Reprocessing by such a CIO can naturally account for the observed UV/optical emission.

6.2. *Origin of the Soft X-ray Emission*

The soft X-ray emission of many TDEs have been attributed to the inner regions of an accretion disk (Saxton et al. 2020). Assuming $R_{\rm in} \approx 6R_{\rm g} \approx 10^{13}$ cm, the maximum effective temperature of an optically thick, geometrially thin accretion disk is $T_{\rm eff} \approx 20(\frac{\dot{m}}{M_7\eta_{-1}})^{1/4}$ eV (Shakura & Sunyaev 1973). With a maximum black hole spin of $a \to 1$, $R_{\rm in} \to R_{\rm g}$, and $T_{\rm eff} \approx 78(\frac{\dot{m}}{M_7\eta_{-1}})^{1/4}$ eV. The top panel of Figure 16 shows that in phase D, when the X-ray spectrum is the hardest, the measured $T_{\rm in}$ is

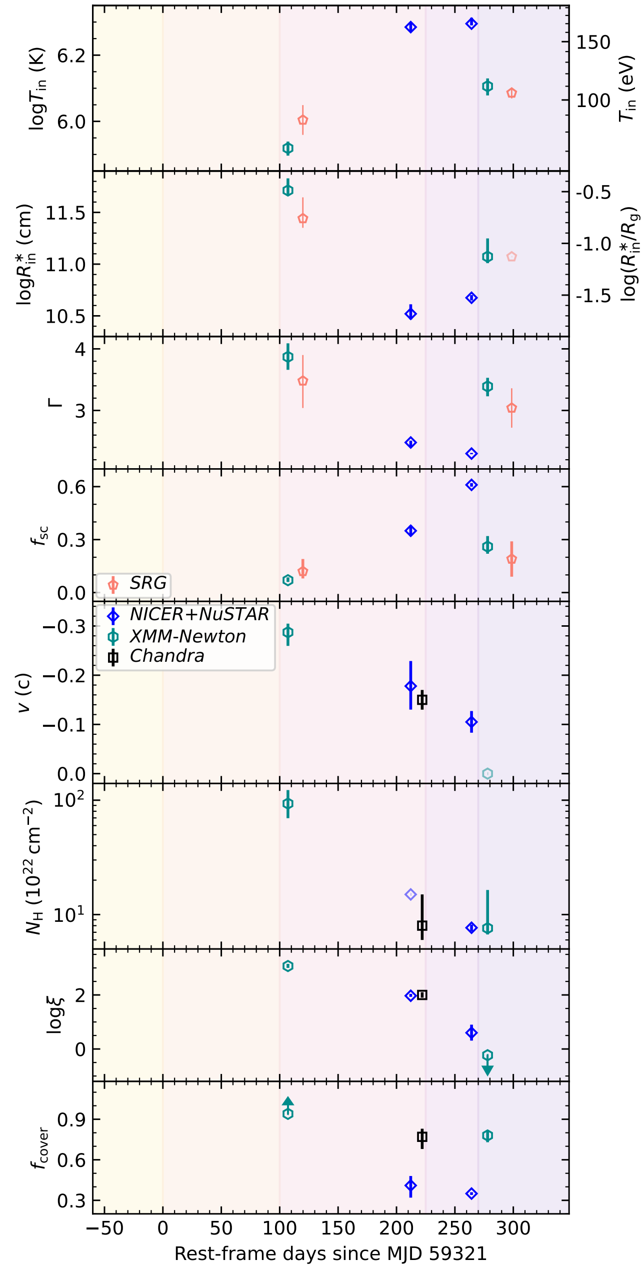

Figure 20. Evolution of best-fit X-ray spectral parameters, including log$T_{\rm in}$ and log$R^*_{\rm in}$ in the `diskbb` component (top two panels), Γ and $f_{\rm sc}$ in the `simpl` component (third–fourth panels), and the four parameters in the `zxipcf` component (bottom four panels, v converted from redshift). Note that the uncertainty of log$(R^*_{\rm in}/R_{\rm g})$ is greater than the uncertainty of $R^*_{\rm in}$ by 0.44 dex (i.e., the uncertainty of $M_{\rm BH}$; §4.1), which is not included in the figure. Data are from model (1c) in Table 3, model (2c) in Table 4, model (3c) and (4c) in Table 5, §5.4.4, and Miller et al. (2022). Fixed values are shown in semi-transparent. Background colors follow the scheme shown in Figure 16.

~ 2 times greater than the maximum allowed $T_{\rm eff}$. A possible reason for this discrepancy is Compton scattering (Shimura & Takahara 1995), which makes the measured temperature to be greater than the effective inner disk temperature by a factor of $f_c \sim 2$ (Davis & El-Abd 2019), i.e., $T_{\rm in} = f_c T_{\rm eff}$.

The inclination of AT2021ehb should not be extremely edge-on (i.e., $\sqrt{\cos i} \gtrsim 0.8$), otherwise the inner X-rays will be mostly obscured by disk materials at larger radii. Moreover, due to the Compton scattering effect mentioned above, the inferred $R_{\rm in}$ is $f_c^2 \sim 4$ times smaller than the actual inner disk radius $R_{\rm d,in}$. The second panel of Figure 16 shows that the ratio between $R_{\rm d,in} \sim 5R^*_{\rm in}$ and $R_{\rm g}$ ranges between 0.1 (in model 1c) and 1.6 (in model 3c).

We note that disk radii much less than $R_{\rm g}$ have also been inferred in a few other X-ray bright TDEs (see, e.g., Fig. 8 of Gezari 2021). A probable explanation is that reprocessing by an ionized medium (e.g., the UFO discussed in §6.1) both enhances the optical flux and suppresses the X-ray flux, with no strong wavelength dependent signature that would show up in the X-ray model fitting (see, e.g., Fig. 5 of Dai et al. 2018).

6.3. *Implications of the hard X-ray emission*

Hard X-rays can be generated by Compton up-scattering of soft X-rays from the accretion disk by the hot electrons in the (magnetically dominated) coronal regions above the disk, as is the case in AGNs and XRBs. The physical situation in TDEs is more complicated than in AGN in that the hard X-rays must make their way out of the complex hydrodynamic structures. An X-ray photon undergoes $\sim \tau^2$ electron scatterings as it propagates through a gas slab of Thomson optical depth τ. In each scattering, the photon loses a fraction $E_\gamma/m_e c^2$ of its energy (where E_γ is the photon energy) as a result of Compton recoil, and hence the cumulative fractional energy loss is $\sim \tau^2 E_\gamma/m_e c^2$. This means that photons above an energy threshold of $\sim 1\,{\rm keV}(\tau/20)^{-2}$ will be Compton down-scattered by the gas.

Our *NuSTAR* observations clearly detected hard X-ray photons up to 30 keV, which requires that the optical depth along the pathways of these photons from the inner disk ($\gtrsim R_{\rm g} \sim 10^{12.2}$ cm) to the observer is less than about 4. On the other hand, the UV/optical emission indicates that the reprocessing layer is optically thick up to a radius of the order $R_{\rm bb} \sim 10^{14}$ cm.

If this reprocessing gas is in the form of a CIO, a scenario that was favored in §6.1, then the center of the CIO must be offset from the central MBH by $\gtrsim 10^{14}$ cm. In line of sights that go through both the CIO and the MBH, the scattering optical depths are large such that the hard X-ray cannot escape. However, in directions where the MBH is not entirely blocked by the CIO, the gas has low column density and hard X-rays can make their way through. Therefore, our observations favor a highly non-spherical system.

6.4. *The Disk–Corona Evolution*

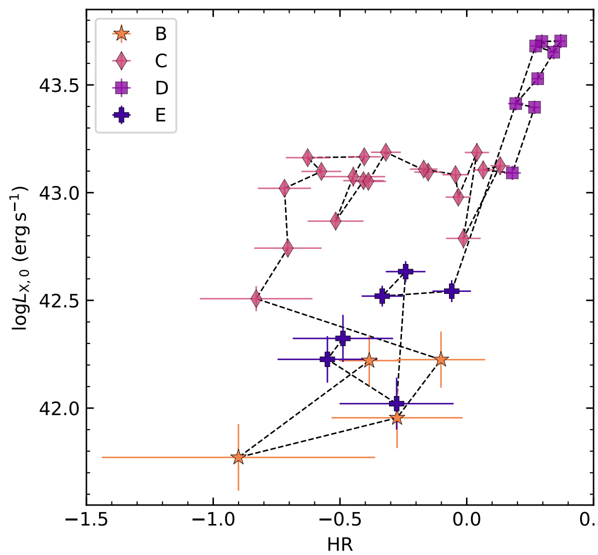

Figure 21. Galactic extinction corrected 0.3–10 keV X-ray luminosity ($L_{\rm X,0}$) as a function of hardness ratio for *Swift*/XRT detections only. The X-ray luminosity of AT2021ehb is the highest when the spectrum is the hardest, a property that is different from XRBs (Remillard & McClintock 2006; Tetarenko et al. 2016), X-ray bright AGNs (Auchettl et al. 2018), CLAGNs (Ruan et al. 2019), and many other X-ray bright TDEs (Wevers 2020; Hinkle et al. 2021).

In stellar mass black hole binary outbursts, some objects are observed to transition between a soft disk-dominated state (SDS) to a hard Comptonized state (HCS), with a transition luminosity of $\lambda_{\rm Edd} = 10^{-1.50\pm0.37}$ (see Fig. 14 of Tetarenko et al. 2016). The $\log\lambda_{\rm Edd}$–$\alpha_{\rm OX}$ diagram has been used by Wevers et al. (2021) to study the evolution of the disk–corona system in the TDE AT2018fyk, which also exhibited a soft → hard spectral transition in the X-ray band. The authors show that the transition luminosity is $L_{\rm bol}/L_{\rm Edd} \sim$ few $\times 10^{-2}$, a value that is similar to the transition $\lambda_{\rm Edd}$ observed in stellar mass black hole binaries. We note that Wevers et al. (2021) consider the 2500 Å emission to mainly trace the outer radii of a viscously heated accretion disk, and the 2 keV emission to track up-scattered photons in the hot corona. However, in §6.1, we favor a reprocessing origin for the UV/optical emission of AT2021ehb. Therefore, we point out the potential caveat of using $f_\nu(2500\,\text{Å})$ as a proxy for AT2021ehb's disk emission.

Wevers (2020) constructed the log$\lambda_{\rm Edd}$–$\alpha_{\rm OX}$ diagram for a sample of 7 X-ray bright TDEs, finding that the 2 keV (corona) emission is stronger when $\lambda_{\rm Edd}$ is lower. Figure 19 shows that this is clearly not the case for AT2021ehb. Separately, Hinkle et al. (2021) studied the evolution of AT2019azh on the canonical hardness–intensity diagram (HID), showing that when the X-ray luminosity is higher, the X-ray spectrum is softer — a behaviour that is similar to that seen in highly variable, X-ray bright AGNs (Auchettl et al. 2018). In Figure 21, we show that AT2021ehb does not follow this trend either.

It is interesting to speculate the reason of the dissimilarities observed between AT2021ehb and other black hole accreting systems. In the SDS of XRBs, the inner radius of the accretion disk $R_{\rm in,d}$ stays around the innermost stable circular orbit (ISCO) of $R_{\rm ISCO} \sim$ few $\times\, R_{\rm g}$. When the outbursts transition to the HCS, $R_{\rm in,d}$ progressively moves outwards to $\sim$ few $\times\, 100R_{\rm g}$, and a region of hot corona is formed close to the BH (Yuan et al. 2005; Done et al. 2007; Yuan & Narayan 2014; Yao et al. 2021b,c), making the disk emission fainter and the non-thermal emission brighter. However, in a TDE hosted by a BH with $M_7 \sim 1$, while the accretion disk is still being circularized, the inner disk can hardly be truncated at $> R_{\rm T} \approx 10R_{\rm g}$. The top two panels of Figure 20 show that when Comptonization is strongest (phase D), the inner disk radius $R_{\rm d,in} \sim 5R^*_{\rm in}$ actually moves inward, and the inner disk temperature $T_{\rm eff} \sim T_{\rm in}/2$ becomes hotter. This unusual property might be related to the real-time formation of an accretion disk.

6.5. *The Lack of Broad Optical Lines*

As is shown in §5.2, AT2021ehb's optical spectroscopic properties are dissimilar to the majority of previously known TDEs (i.e., H-rich, He-rich, N-rich, Fe-rich; Leloudas et al. 2019; van Velzen et al. 2021; Wevers et al. 2019b). It is most similar to a few recently reported TDEs with blue and featureless spectra (Brightman et al. 2021; Hammerstein et al. 2022). Hammerstein et al. (2022) found that compared with TDEs that develop broad emission lines, the UV/optical emission of these four events have larger peak $L_{\rm bb}$, peak $T_{\rm bb}$, and peak $R_{\rm bb}$.

Figure 22 compares the rest-frame g-band light curve of AT2021ehb with 30 TDEs from phase-I of ZTF (Hammerstein et al. 2022). Solid lines are the results of fitting the multi-band light curves ($\delta t < 100$ days) with a Gaussian rise + expotential decay model (see Section 5.1 of van Velzen et al. 2021). We highlight the TDE-featureless class by plotting the data points. Here we have chosen an observing band with good temporal sampling, and converted the observations in this band into $\nu_0 = 6.3 \times 10^{14}$ Hz by performing a color correction.

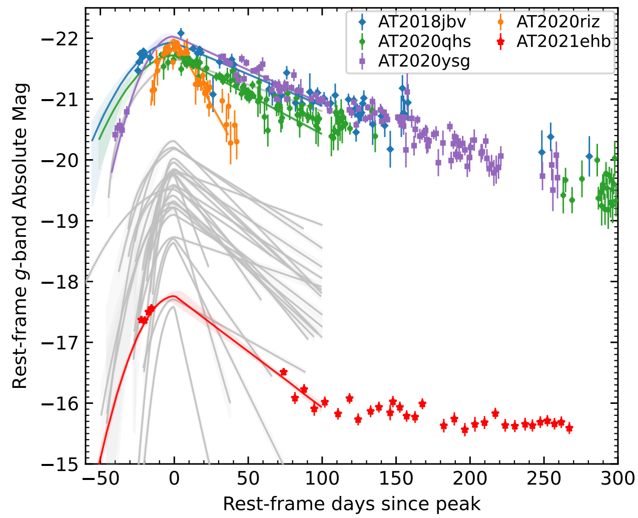

Figure 22. Rest-frame g-band light curve of AT2021ehb compared with that of the 30 TDEs presented by Hammerstein et al. (2022). The solid lines show the best-fit models (see §6.5 for details). Data points are only shown for TDEs with no discernible optical broad lines.

Our study suggests that not all objects in the TDE-featureless class are overluminous. In fact, the peak g-band magnitude ($M_{g,\rm peak}$) and peak $L_{\rm bb}$ of AT2021ehb are small compared with other optically selected TDEs (Figure 5, Figure 22). It is unclear whether $M_{g,\rm peak}$ of the TDE-featureless class spans a large range of values, or clusters at the extreme values (≈ -17 and ≈ -22). This question will be addressed in a forthcoming publication (Yao et al. in prep). A detailed analysis of Hubble Space Telescope (*HST*) UV spectroscopy (Hammerstein et al. in prep) will be essential to reveal if AT2021ehb exhibits any spectral lines in the UV.

7. CONCLUSION

We have presented an extensive X-ray, UV, and optical study of the TDE AT2021ehb. Its peak X-ray flux of ~ 1 mCrab is brighter than any other non-jetted TDEs in the literature, and allowed us to obtain a series of high-quality X-ray spectra, including the first hard X-ray spectrum of a non-jetted TDE up to 30 keV. The detection of hard X-ray photons favor an asymmetric geometry (§6.3). Spectral modeling of the X-ray data yielded detections of blueshifted absorption features from an ionized material, supporting the existence of an UFO. The UFO is likely produced by a stream self collision shock formed as a result of general relativistic apsidal precession. An outflow launched directly from the accretion disk is not favored, because the required minimum launching radius is much greater than the tidal radius of $\sim 10^{13.2}$ cm.

In the stream self-collision scenario, the delayed brightening of AT2021ehb's X-ray emission might signature the delayed formation of an accretion disk, where the disk material comes from the stellar debris plunged from the stream self-collision point. The emission from the self-collision shock itself might contribute to the early-time UV/optical emission, while the post-peak (phase C–E) emission is dominated by reprocessing of X-ray photons in the outflow. More detailed hydrodynamic and radiative transfer calculations (e.g., Roth et al. 2016) are needed to test if this scenario can reproduce the observed UV/optical plateau and the featureless optical spectra.

We observed a soft $\rightarrow$ hard $\rightarrow$ soft spectral transition in the X-ray. The initial soft-to-hard transition happened gradually over ~ 170 days, and might be a result of stronger Comptonization in a newly formed hot corona. The latter hard-to-soft transition happened drastically within 3 days, and the triggering mechanism is subject to future work. Intriguingly, the bolometric luminosity of AT2021ehb is the highest when the X-ray spectrum is the hardest — a property that is different from XRBs, X-ray bright AGNs, and many other TDEs. A possible explanation is that the inner radius of the accretion disk moves inwards as the disk evolves, which both make the disk emission to be hotter, and provide more seed photons to be upscattered.

Systems similar to AT2021ehb are excellent target for X-ray telescopes to study the real-time formation of accretion disks around MBHs, and the interplay between the disk, corona, and the outflow. Detailed understanding of the UFO will be particularly exciting for future X-ray missions with high-resolution spectroscopy, such as *XRISM* (XRISM Science Team 2020) and *Athena* (Barret et al. 2018).

Acknowledgements – We are grateful to the *NuSTAR*, *NICER*, *Swift*, and *XMM-Newton* teams for making this observing campaign possible. Thank Renee, Gullo, Riley for helpful discussions on the *NuSTAR* and *NICER* spectral fitting. Thank Murray for discussions of disk reflection and accretion. Thank Hannah Earnshaw & Dom for discussion on super-Eddington accretion.

Y. Yao acknowledges support from NASA under award No. 80NSSC22K0574.

This work is based on observations obtained with the Samuel Oschin Telescope 48-inch and the 60-inch Telescope at the Palomar Observatory as part of the Zwicky Transient Facility project. ZTF is supported by the National Science Foundation under Grant No. AST-2034437 and a collaboration including Caltech, IPAC, the Weizmann Institute for Science, the Oskar Klein Center at Stockholm University, the University of Maryland, Deutsches Elektronen-Synchrotron and Humboldt University, the TANGO Consortium of Taiwan, the University of Wisconsin at Milwaukee, Trinity College Dublin, Lawrence Livermore National Laboratories, and IN2P3, France. Operations are conducted by COO, IPAC, and UW. The ZTF forced-photometry service was funded under the Heising-Simons Foundation grant #12540303 (PI: Graham).

SED Machine is based upon work supported by the National Science Foundation under Grant No. 1106171.

This work is using observations with eROSITA telescope onboard *SRG* observatory. The *SRG* observatory was built by Roskosmos with the participation of the Deutsches Zentrum für Luft- und Raumfahrt (DLR). The *SRG*/eROSITA X-ray telescope was built by a consortium of German Institutes led by MPE, and supported by DLR. The *SRG* spacecraft was designed, built, launched and is operated by the Lavochkin Association and its subcontractors. The eROSITA data used in this work were processed using the eSASS software system developed by the German eROSITA consortium and proprietary data reduction and analysis software developed by the Russian eROSITA Consortium.

This work made use of data supplied by the UK Swift Science Data Centre at the University of Leicester.

Software: `astropy` (Astropy Collaboration et al. 2013), `emcee` (Foreman-Mackey et al. 2013), `LPipe` (Perley 2019), `matplotlib` (Hunter 2007), `Prospector` (Johnson et al. 2021), `python-fsps` (Foreman-Mackey et al. 2014), `scipy` (Virtanen et al. 2020)

Facilities: XMM, PO:1.2m, Keck:I (LRIS), Keck:II (ESI)

APPENDIX

A. SUPPLEMENTARY TABLES

A.1. *Photometry and Observing Logs*

UV and optical photometry are presented in Table 6. *Swift*/XRT observations are summarized in Table 7.

Table 6. UV and optical photometry of AT2021ehb.

MJD	Instrumnt	Filter	f_ν (μJy)	σ_{f_ν} (μJy)
59250.1643	ZTF	r	-3.04	12.77
59250.2031	ZTF	g	1.89	10.94
59299.0783	UVOT	$uvw1$	567.68	27.76
59299.0798	UVOT	U	551.85	41.60
59299.0808	UVOT	B	487.52	76.95
59299.0831	UVOT	$uvw2$	587.34	22.36
59299.0855	UVOT	V	260.66	146.91
59299.0875	UVOT	$uvm2$	528.68	19.49

Note—f_ν is observed flux density before extinction correction. (This table is available in its entirety in machine-readable form.)

A.2. *X-ray Model Fits*

The XRT spectral parameters are presented in Table 8.

B. OPTICAL SPECTROSCOPY INSTRUMENTAL/OBSERVATIONAL INFORMATION

A log of optical spectroscopic observation is given in Table 9.

For LRIS observations we use the 560 dichroic, the 400/3400 grism on the blue side, the 400/8500 grating on the red side, and the 1″ slit width, which gives $\sigma_{\rm inst} \approx 173\,{\rm km\,s^{-1}}$ on the blue side and $\sigma_{\rm inst} \approx 126\,{\rm km\,s^{-1}}$ on the red side. The LRIS spectra were reduced and extracted using `Lpipe` (Perley 2019).

For DBSP observations we use the D-55 dichroic filter, the 600/4000 grating on the blue side, the 316/7500 grating on the red side. With a slit width of 1.5″ (2.0″), this gives $\sigma_{\rm inst} \approx 106\,{\rm km\,s^{-1}}$ ($\sigma_{\rm inst} \approx 141\,{\rm km\,s^{-1}}$) on the blue side and $\sigma_{\rm inst} \approx 143\,{\rm km\,s^{-1}}$ ($\sigma_{\rm inst} \approx 190\,{\rm km\,s^{-1}}$) on the red side. The DBSP spectra were reduced using the `dbsp_drp` pipeline (Roberson 2021), which is based on `PypeIt` (Prochaska et al. 2020).

The ESI observation was performed in the Echellette mode with a 0.75″ slit, which gives a resolving power of $R = 5350$ (i.e., $\sigma_{\rm inst} = 24\,{\rm km\,s^{-1}}$). The ESI spectrum was reduced using the `MAKEE` pipeline following standard procedures. Flux calibration was not performed. We normalized the spectra by fitting third-order cubic splines to the continuum, with prominent emission and absorption lines masked.

Observations with DeVeny were performed with the 300/4000 grating, with a grating tilt angle of 23.13° to yield a central wavelength of 5800 Å, the clear rear filter, and a slit width of 1.5″. This gives $\sigma_{\rm inst} \approx 169\,{\rm km\,s^{-1}}$. DeVeny spectra were reduced with `PyRAF`, including bias correction and flat-fielding.

REFERENCES

Alam, S., Albareti, F. D., Allende Prieto, C., et al. 2015, ApJS, 219, 12, doi: 10.1088/0067-0049/219/1/12

Anders, E., & Grevesse, N. 1989, GeoCoA, 53, 197, doi: 10.1016/0016-7037(89)90286-X

Table 7. Log of *Swift*/XRT observations of AT2021ehb.

obsID	Start Date	δt (days)	Exp. (s)	Net Count Rate (count s^{-1})	f_X (10^{-13} erg s^{-1} cm^{-2})	$f_{X,0}$ (10^{-13} erg s^{-1} cm^{-2})
14217001	2021-03-26.0	−21.6	2669	< 0.0019	< 0.66	< 1.25
14217003	2021-03-28.2	−19.4	1475	< 0.0027	< 0.96	< 1.82
14217004	2021-03-31.0	−16.7	1683	< 0.0024	< 0.84	< 1.59
14217005	2021-04-02.0	−14.7	1336	< 0.0030	< 1.06	< 2.01
14217006	2021-07-01.2	+73.9	4078	0.0339 ± 0.0029	12.01 ± 3.21	22.73 ± 6.08
14217007	2021-07-09.8	+82.3	1366	0.0120 ± 0.0030	4.27 ± 1.52	8.08 ± 2.88
14217008	2021-07-16.1	+88.5	1348	0.0184 ± 0.0037	6.52 ± 2.11	12.34 ± 4.00
14217009	2021-07-23.1	+95.4	1141	0.0343 ± 0.0056	12.13 ± 3.65	22.96 ± 6.90
14217010	2021-07-30.1	+102.3	1366	0.0502 ± 0.0061	16.57 ± 2.23	44.04 ± 5.92
14217011	2021-08-08.1	+111.1	1925	0.0863 ± 0.0067	28.44 ± 2.76	75.62 ± 7.34
14217012	2021-08-15.9	+118.8	1653	0.1635 ± 0.0100	53.90 ± 4.54	143.32 ± 12.08
14217013	2021-08-22.1	+124.8	2065	0.1958 ± 0.0098	64.56 ± 4.94	171.64 ± 13.13
14217014	2021-08-30.9	+133.5	1583	0.2268 ± 0.0120	74.78 ± 5.87	198.82 ± 15.61
14217015	2021-09-05.5	+139.0	1830	0.2548 ± 0.0119	94.07 ± 7.27	200.69 ± 15.51
14217016	2021-09-12.8	+146.2	641	0.2061 ± 0.0180	76.09 ± 8.13	162.34 ± 17.35
14217017	2021-09-15.0	+148.4	1503	0.1281 ± 0.0093	47.29 ± 4.51	100.90 ± 9.63
14217018	2021-09-19.7	+153.0	1580	0.1974 ± 0.0112	72.90 ± 6.12	155.52 ± 13.05
14217019	2021-09-24.2	+157.4	2045	0.1959 ± 0.0098	72.33 ± 5.76	154.31 ± 12.28
14217020	2021-09-30.4	+163.5	1867	0.2675 ± 0.0120	98.74 ± 7.54	210.67 ± 16.09
14217021	2021-10-05.5	+168.5	1595	0.2775 ± 0.0132	104.81 ± 9.01	170.40 ± 14.65
14217022	2021-10-20.2	+182.9	1618	0.2865 ± 0.0134	108.22 ± 9.24	175.94 ± 15.02
14217023	2021-10-27.4	+190.0	1480	0.2698 ± 0.0136	101.93 ± 8.91	165.71 ± 14.48
14217024	2021-11-03.5	+197.0	2010	0.2124 ± 0.0103	80.23 ± 6.94	130.44 ± 11.29
14217025	2021-11-10.7	+204.0	1286	0.3132 ± 0.0157	149.64 ± 15.02	210.15 ± 21.10
14217026	2021-11-17.2	+210.4	1813	0.1251 ± 0.0084	59.75 ± 6.57	83.92 ± 9.23
14217027	2021-11-24.7	+217.7	1957	0.2718 ± 0.0119	129.86 ± 12.64	182.38 ± 17.75
14217028	2021-12-01.5	+224.4	1967	0.2600 ± 0.0116	124.20 ± 12.14	174.42 ± 17.05
14217029	2021-12-08.1	+230.9	2317	0.2596 ± 0.0107	126.84 ± 9.59	168.93 ± 12.77
14217030	2021-12-15.2	+237.9	2010	0.5234 ± 0.0162	255.79 ± 18.06	340.66 ± 24.05
14217031	2021-12-20.3	+242.9	1293	0.5445 ± 0.0206	266.11 ± 19.65	354.40 ± 26.17
14217032	2021-12-25.6	+248.2	1395	0.7108 ± 0.0227	347.35 ± 24.66	462.59 ± 32.84
14217033	2021-12-30.5	+253.0	1371	0.9721 ± 0.0268	551.93 ± 41.79	691.67 ± 52.37
14217034	2022-01-04.5	+257.8	1410	0.9675 ± 0.0263	549.33 ± 41.53	688.41 ± 52.05
14217035	2022-01-09.2	+262.4	1361	0.8629 ± 0.0253	489.92 ± 37.43	613.96 ± 46.91
14217036	2022-01-14.7	+267.9	1423	0.9218 ± 0.0256	523.38 ± 39.68	655.88 ± 49.72
14217041	2022-02-23.1	+306.6	2594	0.0745 ± 0.0054	26.05 ± 3.06	47.73 ± 5.60
14217042	2022-03-02.2	+313.5	3888	0.0706 ± 0.0043	24.72 ± 2.73	45.29 ± 5.01
14217043	2022-03-09.7	+320.9	2766	0.0918 ± 0.0058	32.11 ± 3.59	58.83 ± 6.58
14217044	2022-03-16.1	+327.2	2956	0.0122 ± 0.0022	5.03 ± 1.40	14.35 ± 3.98
14217045	2022-03-23.0	+334.0	3263	0.0197 ± 0.0025	8.08 ± 2.01	23.04 ± 5.73
14217046	2022-03-30.5	+341.3	2354	0.0246 ± 0.0033	10.11 ± 2.55	28.81 ± 7.26

NOTE—All measurements are given in 0.3–10 keV. f_X and $f_{X,0}$ are converted using the scaling factors derived in Table 8.

Arnaud, K. A. 1996, in Astronomical Society of the Pacific Conference Series, Vol. 101, Astronomical Data Analysis Software and Systems V, ed. G. H. Jacoby & J. Barnes, 17

Astropy Collaboration, Robitaille, T. P., Tollerud, E. J., et al. 2013, A&A, 558, A33, doi: 10.1051/0004-6361/201322068

Auchettl, K., Ramirez-Ruiz, E., & Guillochon, J. 2018, ApJ, 852, 37, doi: 10.3847/1538-4357/aa9b7c

Baldassare, V. F., Dickey, C., Geha, M., & Reines, A. E. 2020, ApJL, 898, L3, doi: 10.3847/2041-8213/aba0c1

Barret, D., Lam Trong, T., den Herder, J.-W., et al. 2018, in Society of Photo-Optical Instrumentation Engineers (SPIE) Conference Series, Vol. 10699, Space Telescopes and Instrumentation 2018: Ultraviolet to Gamma Ray, ed. J.-W. A. den Herder, S. Nikzad, & K. Nakazawa, 106991G, doi: 10.1117/12.2312409

Bellm, E. C., Kulkarni, S. R., Graham, M. J., et al. 2019, PASP, 131, 018002, doi: 10.1088/1538-3873/aaecbe

Table 8. X-ray Fluxes from Modeling of XRT spectra.

Observation	Net 0.3–10 keV Rate	f_ν (0.5 keV)	f_ν (2 keV)	0.3–10 keV $f_{\rm X}$	0.3–10 keV $f_{\rm X,0}$	0.5–10 keV $f_{\rm X,0}$
	(count s^{-1})	(10^{-13} erg s^{-1} cm^{-2})	(10^{-13} erg s^{-1} cm^{-2})	(10^{-13} erg s^{-1} cm^{-2})	(10^{-13} erg s^{-1} cm^{-2})	(10^{-13} erg s^{-1} cm^{-2})
s1	0.0276 ± 0.0019	$2.23^{+0.20}_{-0.36}$	$0.09^{+0.01}_{-0.07}$	$9.76^{+1.39}_{-1.08}$	$18.47^{+2.63}_{-2.05}$	$11.34^{+0.37}_{-2.72}$
s2	0.1476 ± 0.0041	$18.98^{+0.35}_{-1.17}$	$0.31^{+0.02}_{-0.03}$	$48.67^{+1.79}_{-1.03}$	$129.40^{+4.76}_{-2.74}$	$48.96^{+1.34}_{-2.53}$
s3	0.2116 ± 0.0047	$21.52^{+0.56}_{-1.37}$	$0.92^{+0.05}_{-0.05}$	$78.12^{+2.87}_{-1.95}$	$166.66^{+6.13}_{-4.15}$	$86.04^{+1.75}_{-3.95}$
s4	0.2584 ± 0.0062	$14.90^{+0.44}_{-1.34}$	$1.61^{+0.08}_{-0.10}$	$97.63^{+3.67}_{-3.31}$	$158.72^{+5.97}_{-5.37}$	$109.87^{+2.56}_{-5.73}$
s5	0.2382 ± 0.0058	$10.80^{+0.42}_{-1.15}$	$2.00^{+0.09}_{-0.16}$	$113.80^{+5.90}_{-4.00}$	$159.82^{+8.29}_{-5.62}$	$127.47^{+3.50}_{-7.81}$
s6	0.4776 ± 0.0083	$17.08^{+0.62}_{-2.09}$	$5.03^{+0.20}_{-0.16}$	$233.38^{+10.02}_{-4.78}$	$310.81^{+13.34}_{-6.37}$	$256.24^{+5.50}_{-11.15}$
s7	0.9314 ± 0.0129	$28.84^{+1.47}_{-2.11}$	$10.56^{+0.26}_{-0.48}$	$528.81^{+22.79}_{-14.51}$	$662.69^{+28.56}_{-18.18}$	$579.24^{+14.10}_{-27.91}$
s8	0.0780 ± 0.0029	$5.60^{+0.24}_{-0.69}$	$0.39^{+0.03}_{-0.04}$	$27.30^{+1.56}_{-0.96}$	$50.03^{+2.85}_{-1.77}$	$30.99^{+1.06}_{-2.74}$
s9	0.0185 ± 0.0015	$2.40^{+0.01}_{-1.46}$	$0.08^{+0.02}_{-0.01}$	$7.59^{+1.11}_{-0.52}$	$21.62^{+3.15}_{-1.48}$	$6.78^{+0.48}_{-1.38}$

Note—f_ν(0.5 keV), f_ν(2 keV), and $f_{\rm X,0}$ are the Galactic absorption corrected fluxes; $f_{\rm X}$ is the observed flux.

Table 9. Log of AT2021ehb optical spectroscopy.

Start Date	δt (days)	Telescope	Instrument	Wavelength range (Å)	Slit width (″)	Exp. (s)
2021-03-25.1	−22	P60	SEDM	3770–9223	—	2160
2021-03-27.1	−20	P60	SEDM	3770–9223	—	2160
2021-07-06.6	+79	Keck-I	LRIS	3200–10250	1.0	300
2021-08-01.4	+104	P200	DBSP	3410–5550, 5750–9995	1.5	900
2021-08-13.6	+116	Keck-I	LRIS	3200–10250	1.0	300
2021-09-07.6	+141	Keck-I	LRIS	3200–10250	1.0	300
2021-09-17.4	+150	P60	SEDM	3770–9223	—	2700
2021-10-27.5	+190	LDT	DeVeny	3586–8034	1.5	2400
2021-11-13.3	+206	P60	SEDM	3770–9223	—	2700
2021-12-03.3	+226	P60	SEDM	3770–9223	—	2700
2021-12-28.4	+250	Keck-II	ESI	4000–10250	0.75	300
2022-01-05.2	+258	P60	SEDM	3770–9223	—	2700
2022-01-12.2	+265	P200	DBSP	3410–5550, 5750–9995	2.0	600
2022-01-20.3	+273	P60	SEDM	3770–9223	—	2700
2022-01-27.3	+280	P60	SEDM	3770–9223	—	2700
2022-02-06.3	+290	Keck-I	LRIS	3200–10250	1.0	300
2022-03-27.1	+338	P200	DBSP	3410–5550, 5750–9995	1.5	1200

Note—All spectra will be made available on the TNS page of this source (https://www.wis-tns.org/object/2021ehb) at the time of manuscript submission.

Blagorodnova, N., Neill, J. D., Walters, R., et al. 2018, PASP, 130, 035003, doi: 10.1088/1538-3873/aaa53f

Blanchard, P. K., Nicholl, M., Berger, E., et al. 2017, ApJ, 843, 106, doi: 10.3847/1538-4357/aa77f7

Bonnerot, C., Lu, W., & Hopkins, P. F. 2021, MNRAS, 504, 4885, doi: 10.1093/mnras/stab398

Bonnerot, C., Rossi, E. M., Lodato, G., & Price, D. J. 2016, MNRAS, 455, 2253, doi: 10.1093/mnras/stv2411

Brightman, M., Ward, C., Stern, D., et al. 2021, ApJ, 909, 102, doi: 10.3847/1538-4357/abde34

Burrows, D. N., Hill, J. E., Nousek, J. A., et al. 2005, SSRv, 120, 165, doi: 10.1007/s11214-005-5097-2

Cappellari, M. 2017, MNRAS, 466, 798, doi: 10.1093/mnras/stw3020

Cappellari, M., & Emsellem, E. 2004, PASP, 116, 138, doi: 10.1086/381875

Cardelli, J. A., Clayton, G. C., & Mathis, J. S. 1989, ApJ, 345, 245, doi: 10.1086/167900

Cenko, S. B., Fox, D. B., Moon, D.-S., et al. 2006, PASP, 118, 1396, doi: 10.1086/508366

Conroy, C., Gunn, J. E., & White, M. 2009, ApJ, 699, 486, doi: 10.1088/0004-637X/699/1/486

Curd, B., & Narayan, R. 2019, MNRAS, 483, 565, doi: 10.1093/mnras/sty3134

Cutri, R. M., & et al. 2013, VizieR Online Data Catalog, II/328

Dai, L., McKinney, J. C., & Miller, M. C. 2015, ApJL, 812, L39, doi: 10.1088/2041-8205/812/2/L39

Dai, L., McKinney, J. C., Roth, N., Ramirez-Ruiz, E., & Miller, M. C. 2018, ApJL, 859, L20, doi: 10.3847/2041-8213/aab429

Dálya, G., Galgóczi, G., Dobos, L., et al. 2018, MNRAS, 479, 2374, doi: 10.1093/mnras/sty1703

Davis, S. W., & El-Abd, S. 2019, ApJ, 874, 23, doi: 10.3847/1538-4357/ab05c5

Dekany, R., Smith, R. M., Riddle, R., et al. 2020, Publications of the Astronomical Society of the Pacific, 132, 038001, doi: 10.1088/1538-3873/ab4ca2

Done, C., Gierliński, M., & Kubota, A. 2007, A&A Rv, 15, 1, doi: 10.1007/s00159-007-0006-1

Donley, J. L., Brandt, W. N., Eracleous, M., & Boller, T. 2002, AJ, 124, 1308, doi: 10.1086/342280

Evans, P. A., Beardmore, A. P., Page, K. L., et al. 2009, MNRAS, 397, 1177, doi: 10.1111/j.1365-2966.2009.14913.x

Fabian, A. C. 2016, Astronomische Nachrichten, 337, 375, doi: 10.1002/asna.201612316

Ferrarese, L., & Ford, H. 2005, SSRv, 116, 523, doi: 10.1007/s11214-005-3947-6

Flewelling, H. A., Magnier, E. A., Chambers, K. C., et al. 2020, ApJS, 251, 7, doi: 10.3847/1538-4365/abb82d

Foreman-Mackey, D., Hogg, D. W., Lang, D., & Goodman, J. 2013, Publications of the Astronomical Society of the Pacific, 125, 306, doi: 10.1086/670067

Foreman-Mackey, D., Sick, J., & Johnson, B. 2014, python-fsps: Python bindings to FSPS (v0.1.1), v0.1.1, Zenodo, doi: 10.5281/zenodo.12157

Fremling, C., Sollerman, J., Taddia, F., et al. 2016, A&A, 593, A68, doi: 10.1051/0004-6361/201628275

French, K. D., Wevers, T., Law-Smith, J., Graur, O., & Zabludoff, A. I. 2020, SSRv, 216, 32, doi: 10.1007/s11214-020-00657-y

Gabriel, C., Denby, M., Fyfe, D. J., et al. 2004, in Astronomical Society of the Pacific Conference Series, Vol. 314, Astronomical Data Analysis Software and Systems (ADASS) XIII, ed. F. Ochsenbein, M. G. Allen, & D. Egret, 759

Gendreau, K. C., Arzoumanian, Z., Adkins, P. W., et al. 2016, in Society of Photo-Optical Instrumentation Engineers (SPIE) Conference Series, Vol. 9905, Space Telescopes and Instrumentation 2016: Ultraviolet to Gamma Ray, 99051H, doi: 10.1117/12.2231304

Gezari, S. 2021, ARA&A, 59, doi: 10.1146/annurev-astro-111720-030029

Gezari, S., Cenko, S. B., & Arcavi, I. 2017, ApJL, 851, L47, doi: 10.3847/2041-8213/aaa0c2

Gezari, S., Hammerstein, E., Yao, Y., et al. 2021, Transient Name Server AstroNote, 103, 1

Graham, M. J., Kulkarni, S. R., Bellm, E. C., et al. 2019, PASP, 131, 078001, doi: 10.1088/1538-3873/ab006c

Greene, J. E., Strader, J., & Ho, L. C. 2020, ARA&A, 58, 257, doi: 10.1146/annurev-astro-032620-021835

Guolo, M., Ruschel-Dutra, D., Grupe, D., et al. 2021, MNRAS, 508, 144, doi: 10.1093/mnras/stab2550

Hammerstein, E., van Velzen, S., Gezari, S., et al. 2022, arXiv e-prints, arXiv:2203.01461. https://arxiv.org/abs/2203.01461

Harrison, F. A., Craig, W. W., Christensen, F. E., et al. 2013, ApJ, 770, 103, doi: 10.1088/0004-637X/770/2/103

HI4PI Collaboration, Ben Bekhti, N., Flöer, L., et al. 2016, A&A, 594, A116, doi: 10.1051/0004-6361/201629178

Hinkle, J. T., Holoien, T. W. S., Auchettl, K., et al. 2021, MNRAS, 500, 1673, doi: 10.1093/mnras/staa3170

Hunter, J. D. 2007, Computing In Science & Engineering, 9, 90, doi: 10.1109/MCSE.2007.55

Jiang, Y.-F., Guillochon, J., & Loeb, A. 2016, ApJ, 830, 125, doi: 10.3847/0004-637X/830/2/125

Johnson, B. D., Leja, J., Conroy, C., & Speagle, J. S. 2021, ApJS, 254, 22, doi: 10.3847/1538-4365/abef67

Kaastra, J. S., & Bleeker, J. A. M. 2016, A&A, 587, A151, doi: 10.1051/0004-6361/201527395

Kajava, J. J. E., Giustini, M., Saxton, R. D., & Miniutti, G. 2020, A&A, 639, A100, doi: 10.1051/0004-6361/202038165

Kallman, T., & Bautista, M. 2001, ApJS, 133, 221, doi: 10.1086/319184

Kara, E., Dai, L., Reynolds, C. S., & Kallman, T. 2018, MNRAS, 474, 3593, doi: 10.1093/mnras/stx3004

Kara, E., Miller, J. M., Reynolds, C., & Dai, L. 2016, Nature, 535, 388, doi: 10.1038/nature18007

Kellogg, E., Baldwin, J. R., & Koch, D. 1975, ApJ, 199, 299, doi: 10.1086/153692

Kormendy, J., & Ho, L. C. 2013, ARA&A, 51, 511, doi: 10.1146/annurev-astro-082708-101811

Leloudas, G., Dai, L., Arcavi, I., et al. 2019, ApJ, 887, 218, doi: 10.3847/1538-4357/ab5792

Lin, D., Maksym, P. W., Irwin, J. A., et al. 2015, ApJ, 811, 43, doi: 10.1088/0004-637X/811/1/43

Lu, W., & Bonnerot, C. 2020, MNRAS, 492, 686, doi: 10.1093/mnras/stz3405

Madsen, K. K., Beardmore, A. P., Forster, K., et al. 2017, AJ, 153, 2, doi: 10.3847/1538-3881/153/1/2

Masci, F. J., Laher, R. R., Rusholme, B., et al. 2019, PASP, 131, 018003, doi: 10.1088/1538-3873/aae8ac

Metzger, B. D., & Stone, N. C. 2016, MNRAS, 461, 948, doi: 10.1093/mnras/stw1394

Miller, J. M., Reynolds, M. T., Yun, S. B., et al. 2022, The Astronomer's Telegram, 15179, 1

Mitsuda, K., Inoue, H., Koyama, K., et al. 1984, PASJ, 36, 741

Mummery, A., & Balbus, S. A. 2020, MNRAS, 492, 5655, doi: 10.1093/mnras/staa192

Munoz-Arancibia, A., Forster, F., Bauer, F. E., et al. 2021, Transient Name Server Discovery Report, 2021-651, 1

Nicholl, M., Lanning, D., Ramsden, P., et al. 2022, arXiv e-prints, arXiv:2201.02649. https://arxiv.org/abs/2201.02649

Oke, J. B., & Gunn, J. E. 1982, PASP, 94, 586, doi: 10.1086/131027

Oke, J. B., Cohen, J. G., Carr, M., et al. 1995, PASP, 107, 375, doi: 10.1086/133562

Pasham, D. R., Cenko, S. B., Sadowski, A., et al. 2017, ApJL, 837, L30, doi: 10.3847/2041-8213/aa6003

Pavlinsky, M., Tkachenko, A., Levin, V., et al. 2021, A&A, 650, A42, doi: 10.1051/0004-6361/202040265

Perley, D. A. 2019, PASP, 131, 084503, doi: 10.1088/1538-3873/ab215d

Phinney, E. S. 1989, in The Center of the Galaxy, ed. M. Morris, Vol. 136, 543

Piran, T., Svirski, G., Krolik, J., Cheng, R. M., & Shiokawa, H. 2015, ApJ, 806, 164, doi: 10.1088/0004-637X/806/2/164

Predehl, P., Andritschke, R., Arefiev, V., et al. 2021, A&A, 647, A1, doi: 10.1051/0004-6361/202039313

Prochaska, J. X., Hennawi, J. F., Westfall, K. B., et al. 2020, Journal of Open Source Software, 5, 2308, doi: 10.21105/joss.02308

Prugniel, P., & Soubiran, C. 2001, A&A, 369, 1048, doi: 10.1051/0004-6361:20010163

Prugniel, P., Soubiran, C., Koleva, M., & Le Borgne, D. 2007, arXiv e-prints, astro. https://arxiv.org/abs/astro-ph/0703658

Rees, M. J. 1988, Nature, 333, 523, doi: 10.1038/333523a0

Reeves, J., Done, C., Pounds, K., et al. 2008, MNRAS, 385, L108, doi: 10.1111/j.1745-3933.2008.00443.x

Remillard, R. A., & McClintock, J. E. 2006, ARA&A, 44, 49, doi: 10.1146/annurev.astro.44.051905.092532

Remillard, R. A., Loewenstein, M., Steiner, J. F., et al. 2022, AJ, 163, 130, doi: 10.3847/1538-3881/ac4ae6

Rigault, M., Neill, J. D., Blagorodnova, N., et al. 2019, A&A, 627, A115, doi: 10.1051/0004-6361/201935344

Roberson, M. 2021, DBSP DRP, GitHub. https://github.com/finagle29/dbsp_drp

Roming, P. W. A., Kennedy, T. E., Mason, K. O., et al. 2005, SSRv, 120, 95, doi: 10.1007/s11214-005-5095-4

Rosswog, S., Ramirez-Ruiz, E., & Hix, W. R. 2009, ApJ, 695, 404, doi: 10.1088/0004-637X/695/1/404

Roth, N., Kasen, D., Guillochon, J., & Ramirez-Ruiz, E. 2016, ApJ, 827, 3, doi: 10.3847/0004-637X/827/1/3

Ruan, J. J., Anderson, S. F., Eracleous, M., et al. 2019, ApJ, 883, 76, doi: 10.3847/1538-4357/ab3c1a

Saxton, R., Komossa, S., Auchettl, K., & Jonker, P. G. 2020, SSRv, 216, 85, doi: 10.1007/s11214-020-00708-4

Sazonov, S., Gilfanov, M., Medvedev, P., et al. 2021, MNRAS, 508, 3820, doi: 10.1093/mnras/stab2843

Schlafly, E. F., & Finkbeiner, D. P. 2011, ApJ, 737, 103, doi: 10.1088/0004-637X/737/2/103

Shakura, N. I., & Sunyaev, R. A. 1973, A&A, 24, 337

Sheinis, A. I., Bolte, M., Epps, H. W., et al. 2002, PASP, 114, 851, doi: 10.1086/341706

Shimura, T., & Takahara, F. 1995, ApJ, 445, 780, doi: 10.1086/175740

Skrutskie, M. F., Cutri, R. M., Stiening, R., et al. 2006, AJ, 131, 1163, doi: 10.1086/498708

Steele, I. A., Smith, R. J., Rees, P. C., et al. 2004, in Society of Photo-Optical Instrumentation Engineers (SPIE) Conference Series, Vol. 5489, Ground-based Telescopes, ed. J. Oschmann, Jacobus M., 679–692, doi: 10.1117/12.551456

Stein, R., Velzen, S. v., Kowalski, M., et al. 2021, Nature Astronomy, 5, 510, doi: 10.1038/s41550-020-01295-8

Steiner, J. F., Narayan, R., McClintock, J. E., & Ebisawa, K. 2009, PASP, 121, 1279, doi: 10.1086/648535

Strubbe, L. E., & Quataert, E. 2009, MNRAS, 400, 2070, doi: 10.1111/j.1365-2966.2009.15599.x

Strüder, L., Briel, U., Dennerl, K., et al. 2001, A&A, 365, L18, doi: 10.1051/0004-6361:20000066

Sunyaev, R., Arefiev, V., Babyshkin, V., et al. 2021, arXiv e-prints, arXiv:2104.13267. https://arxiv.org/abs/2104.13267

Tananbaum, H., Avni, Y., Branduardi, G., et al. 1979, ApJL, 234, L9, doi: 10.1086/183100

Tarter, C. B., Tucker, W. H., & Salpeter, E. E. 1969, ApJ, 156, 943, doi: 10.1086/150026

Tetarenko, B. E., Sivakoff, G. R., Heinke, C. O., & Gladstone, J. C. 2016, ApJS, 222, 15, doi: 10.3847/0067-0049/222/2/15

Ulmer, A. 1999, ApJ, 514, 180, doi: 10.1086/306909

van Velzen, S., Gezari, S., Cenko, S. B., et al. 2019, ApJ, 872, 198, doi: 10.3847/1538-4357/aafe0c

van Velzen, S., Gezari, S., Hammerstein, E., et al. 2021, ApJ, 908, 4, doi: 10.3847/1538-4357/abc258

Verner, D. A., Ferland, G. J., Korista, K. T., & Yakovlev, D. G. 1996, ApJ, 465, 487, doi: 10.1086/177435

Virtanen, P., Gommers, R., Oliphant, T. E., et al. 2020, Nature Methods, 17, 261, doi: 10.1038/s41592-019-0686-2

Waters, C. Z., Magnier, E. A., Price, P. A., et al. 2020, ApJS, 251, 4, doi: 10.3847/1538-4365/abb82b

Wevers, T. 2020, MNRAS, 497, L1, doi: 10.1093/mnrasl/slaa097

Wevers, T., van Velzen, S., Jonker, P. G., et al. 2017, MNRAS, 471, 1694, doi: 10.1093/mnras/stx1703

Wevers, T., Stone, N. C., van Velzen, S., et al. 2019a, MNRAS, 487, 4136, doi: 10.1093/mnras/stz1602

Wevers, T., Pasham, D. R., van Velzen, S., et al. 2019b, MNRAS, 488, 4816, doi: 10.1093/mnras/stz1976

—. 2021, ApJ, 912, 151, doi: 10.3847/1538-4357/abf5e2

Wilms, J., Allen, A., & McCray, R. 2000, ApJ, 542, 914, doi: 10.1086/317016

XRISM Science Team. 2020, arXiv e-prints, arXiv:2003.04962. https://arxiv.org/abs/2003.04962

Yao, Y., Brightman, M., Gezari, S., et al. 2021a, Transient Name Server AstroNote, 183, 1

Yao, Y., Pasham, D. R., Gendreau, K. C., et al. 2022, The Astronomer's Telegram, 15217, 1

Yao, Y., Miller, A. A., Kulkarni, S. R., et al. 2019, ApJ, 886, 152, doi: 10.3847/1538-4357/ab4cf5

Yao, Y., De, K., Kasliwal, M. M., et al. 2020, ApJ, 900, 46, doi: 10.3847/1538-4357/abaa3d

Yao, Y., Kulkarni, S. R., Gendreau, K. C., et al. 2021b, ApJ, 920, 121, doi: 10.3847/1538-4357/ac15f8

Yao, Y., Kulkarni, S. R., Burdge, K. B., et al. 2021c, ApJ, 920, 120, doi: 10.3847/1538-4357/ac15f9

Yuan, F., Cui, W., & Narayan, R. 2005, ApJ, 620, 905, doi: 10.1086/427206

Yuan, F., & Narayan, R. 2014, ARA&A, 52, 529, doi: 10.1146/annurev-astro-082812-141003